January 2016

Profile fitting in crowded astronomical images

Raja Manish
Purdue University

Graduate School Form
30 Updated 12/26/2015

PURDUE UNIVERSITY
GRADUATE SCHOOL
Thesis/Dissertation Acceptance

This is to certify that the thesis/dissertation prepared

By RAJA MANISH

Entitled
PROFILE FITTING IN CROWDED ASTRONOMICAL IMAGES

For the degree of Master of Science in Aeronautics and Astronautics

Is approved by the final examining committee:

CAROLIN FRUEH
Chair

INSEOK HWANG

JAMES L. GARRISON

To the best of my knowledge and as understood by the student in the Thesis/Dissertation Agreement, Publication Delay, and Certification Disclaimer (Graduate School Form 32), this thesis/dissertation adheres to the provisions of Purdue University's "Policy of Integrity in Research" and the use of copyright material.

Approved by Major Professor(s): CAROLIN FRUEH

Approved by: WEINONG (WAYNE) CHEN 4/19/2016
Head of the Departmental Graduate Program Date

PROFILE FITTING IN CROWDED ASTRONOMICAL IMAGES

A Thesis

Submitted to the Faculty

of

Purdue University

by

Raja Manish

In Partial Fulfillment of the

Requirements for the Degree

of

Master of Science in Aeronautics and Astronautics

May 2016

Purdue University

West Lafayette, Indiana

To my family

ACKNOWLEDGMENTS

I would like to acknowledge the school of Aeronautics and Astronautics for providing me the opportunity to pursue the major of my interest.

A number of people helped me in my academics in variety of ways. Firstly, I would like to thank my advisor Professor Carolin Frueh for guiding me throughout the research and her timely assistance. I would also like to express my gratitude to other committee members Professor Inseok Hwang and Professor James Garrison for their time and consideration.

I would like to thank Francois Sanson and Nathan Houtz for their help in the research. At the same time Sangjin, Sangjun and Adam kept me motivated with their persuasive words.

Last but not least, I would like to thank my parents and siblings for all their love and support. This work is dedicated to them.

TABLE OF CONTENTS

LIST OF TABLES

LIST OF FIGURES

Figure Page

SYMBOLS

D	Aperture diameter
d	Aperture diameter obstructed due to construction
I	intensity of the source
λ	wavelength of light
h	Plank's constant
e	exponential
C	photon count
S	signal
N	noise
N_{total}	source signal
n_{pix}	total number of pixels in frame
n_B	number of pixels for background calculation
$N_{sky}, N_{digital}, N_{readout}$	Sky, digitization and readout noises respectively
G	gain
$\sigma, \sigma_x, \sigma_y$	RMS half width or spread of the PSF
$V, \hat{Z}$	measurement data
δ	error function
θ	PSF parameter set
L	likelihood
H	Hessian matrix
Σ, K	covariance matrix
F	Fisher information matriix
Z_o	Peak intensity at the mean
u_x, u_y	centroid
x, y	Coordinates, pixels

η	random additive noise
ε	weighted error function
k	iteration index, factor for sigma
ρ	correlation coefficient
e^-	electron charge
c	clipped background
ΔD_{obs}	Difference between observed maximum intensity and mean of intensities around maximum

ABBREVIATIONS

QE	Quantum efficiency
ADU	Analog to digital unit
FWHM	Full width at half maximum
PSF	Point Spread function
LS	least squares
2D	two dimensional
CCD	Charge-coupled device
SNR	Signal-to Noise Ratio
RMS	Root mean square
px	pixel
RA	Right ascension
Dec	Declination
USNO	United States Naval Observatory
HOT	Higher order terms

ABSTRACT

Manish, Raja MSAAE, Purdue University, May 2016. Profile Fitting in Crowded Astronomical Images. Major Professor: Carolin Frueh.

Around 18,000 known objects currently populate the near Earth space. These constitute active space assets as well as space debris objects. The tracking and cataloging of such objects relies on observations, most of which are ground based. Also, because of the great distance to the objects, only non-resolved object images can be obtained from the observations.

Optical systems consist of telescope optics and a detector. Nowadays, usually CCD detectors are used. The information that is sought to be extracted from the frames are the individual object's astrometric position. In order to do so, the center of the object's image on the CCD frame has to be found. However, the observation frames that are read out of the detector are subject to noise. There are three different sources of noise: celestial background sources, the object signal itself and the sensor noise. The noise statistics are usually modeled as Gaussian or Poisson distributed or their combined distribution.

In order to achieve a near real time processing, computationally fast and reliable methods for the so-called centroiding are desired; analytical methods are preferred over numerical ones of comparable accuracy.

In this work, an analytic method for the centroiding is investigated and compared to numerical methods. Though the work focuses mainly on astronomical images, same principle could be applied on non-celestial images containing similar data. The method is based on minimizing weighted least squared (LS) error between observed data and the theoretical model of point sources in a novel yet simple way. Synthetic image frames have been simulated. The newly developed method is tested in both

crowded and non-crowded fields where former needs additional image handling procedures to separate closely packed objects. Subsequent analysis on real celestial images corroborate the effectiveness of the approach.

1. INTRODUCTION

1.1 Motivation and Background

For over five decades, the near Earth space is getting continuously populated with launches of man-made spacecrafts. Currently, around 16,000 known objects orbit the near Earth space. These includes active and inactive spacecrafts, rocket bodies and mission related debris to mention a few [1]. According to USSTRATCOM's Joint Space Operations Center (JSpOC) [2] "About 5 percent of those being tracked are functioning payloads or satellites, 8 percent are rocket bodies, and about 87 percent are debris and/or inactive satellites". Over time, older spacecrafts disintegrate or some of the in-orbit objects collide with each other leading to fragmentations, thereby increasing the number of unknown objects. Some of the recent known fragmentations were due to the Chinese anti-satellite test in 2007 and the Iridium 33 - Russian cosmos 2251 satellite collision in 2009.

The near Earth space can be divided into several regions: the low Earth Orbit (LEO) extending up to 2,000 km altitude, the medium Earth orbit (MEO) from 2,000 km to 35,586 km and the geosynchronous Earth orbit (GEO) from 35,586 km to 35,986 km. Out of all the cataloged objects, about 75% are in the LEO region. Since these objects move at tremendous velocities, result of a collision could be catastrophic for useful payloads. ([3] and the references therein contain more information on the space debris and effects of such collision.) It is therefore essential to locate and catalog these objects.

In order to locate and catalog these objects, we need the centroids of objects' image's along with that of the nearby stars in image for calibration. Also, it is important that the objects are located with accuracies in sub arc-second because for example, in the LEO region, each arc-second correspond to about 50 centimeters of

position inaccuracy while in the geostationary orbit this corresponds to about 174 meters. Sometimes, objects which have poor radar detectability could be optically bright (and vice versa) [4]; an accurate optical-detection system is justified in such scenario.

In this work, an analytic method to determine the centroid of objects from celestial images is investigated. The work is organized as follows. The remaining part of chapter 1 introduces the physical process of image creation. Chapter 2 delineates state of the art algorithms for centroiding and provides a comparison among those methods. In chapter 3, the analytic least squares 2-dimensional approximation (LS 2D) method is developed and expressions for object's parameters are derived. In chapter 4 and 5, synthetic point source as well as crowded source are generated and object centroids are obtained for validation. Chapter 6 describes some of the image handling procedures for celestial images. Lastly, chapter 7 explains the applicability of the algorithm on real celestial images. Then the analysis is finally concluded.

1.2 Physical Processes of Image Creation

1.2.1 The Charge-Coupled Device (CCD)

The charge-coupled devices (CCD) are used as sensors in imaging instruments. CCD detectors works on the principle of photoelectric effect. Light photons of a particular range of wavelengths are easily absorbed by a semi-conductor, like silicon. CCDs made using silicon are most useful at optical wavelengths (3000 Å– 11,000 Å). Incoming photons are absorbed by the silicon causing the latter to release a valence electron to the conduction band. These electrons in the conduction band are then collected from across various pixels and readout at the end of exposure. A change in voltage potential allows the charge to transfer from one location to another. This charge is then amplified, processed through an analog to digital transformer and stored.

Modern CCDs can reach a quantum efficiencies of about 97 percent. Quantum efficiency is the ratio of photons stored to the incoming photons. Several flaws in the CCD contribute to electron losses and spurious electrons' addition. The charge transfer is not perfect. It has an efficiency (percentage charge transferred to charge collected) of about 99.9999%. Some of the electrons diffuse into their neighboring pixels before they are collected. Furthermore, the integrated circuit construction, size of the amplifier and its temperature contribute to the addition of certain electrons commonly known as readout noise. The process of analog-to-digital conversion also introduces an uncertainty known as truncation error. The thermal agitation of the CCD material causes the emission of electrons even in complete darkness or when the camera shutter is never opened. They are referred to as the dark noise. Such type of noise can be reduced by cooling the CCD.

(a) (b)

Figure 1.1. (a) Array of 30 CCDs used on Sloan Digital Sky Survey (SDSS) telescope imaging camera. [6]. (b) A telescope-CCD camera setup [7]

Once the pixel values are stored after digitization, a raw image is generated. In order to extract the signal of an object of interest, the background or "sky" must be subtracted. The background in a CCD image contains light signal from stars, scattered lights and other celestial bodies as well as read noise, dark noise and other sources. [5] (More details on background estimation is in section 6.2).

CCDs are widely employed and preferred in astronomical applications owing to their high quantum efficiency compared to some other types of sensors (like photographic plates). The important properties of a sensor like the size of individual pixel, packing of the mosaic, quantum efficiency, sensitivity, limits etc. are generally available in the specification sheet supplied by the manufacturer. However, other informations like image compression, frame and data transfer rates depends on the processing unit that may or may not be supplied with the sensor. When a CCD camera is used in conjunction with a telescope, the field of view (FOV) ranges between half a square degree to up to 8×8 degrees whereas the pixel scales can vary from 0.5 arc-second to several arc-seconds per pixel [8]. Comprehensive details on CCDs can be found in [5].

1.2.2 Noise and its Sources - Celestial and Sensor

Noises in images from telescopes are due to the celestial background and the sensor. Celestial sources can be diffused and discrete. Diffused sources include airglow, scattered light and faint stars while discrete sources are zodiacal light, moonlight, stars, galaxies, nebulae, artificial satellite etc [9]. Due to the varying nature of the light photons striking the detector array, celestial background noise can be modeled as Poisson distributed. This sometimes depend on the instrument's field of view in the sense that there can be a magnitude below which a star could not be resolved by the detector as a discrete object and hence consider that as a diffused source [9]. An example would be a large FOV of the telescope. In celestial imaging, the pixel scale of CCD is given by arc-second per pixel. When the FOV is very large, the amount of celestial data fitted in each pixel is increased, thus leading to loss in resolution. Hence, the instrument would fail to separate the finer celestial objects and instead treat them as a diffused source.

Figure 1.2. The Mauna Kea observatories, Hawaii [10]. Observatories are located at high altitudes far from major population, to minimize the effect of scattered lights.

On the other hand, sensor noises such as dark, readout, truncation etc. are due to the properties of CCD and its operation. These noises can be minimized by certain means. For example, the dark noise as discussed in the previous section can be minimized by cooling the CCD.

Both the celestial background and the dark noise depend on the integration time of the detector (equation 1.1.) The longer the detector is exposed to the light, the higher will be the background and dark noise photon counts along with the useful signal. Fig. 1.3 shows the block diagram of a typical imaging system along with the

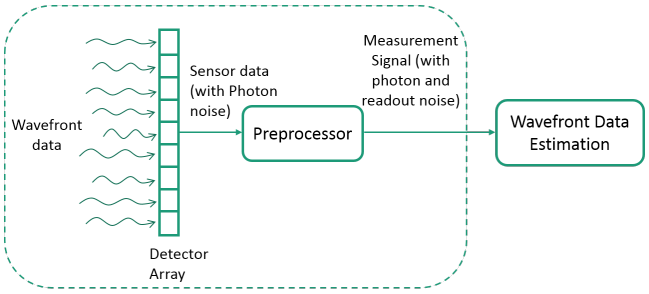

Figure 1.3. Block diagram of an imaging system with signal flow [11]

propagation of noise. When electrons across the sensor are collected and processed by

the preprocessor, a constant Gaussian noise is added to the signal. Source parameters are then estimated from this combined measurement data.

1.2.3 Sensor Counts

Images obtained from the optical imaging systems provide useful information for the astrometric position of the stars and the object of interest. However, these images are non-resolved because of the large distance between the observer and the object of interest. Also, there are noises generated by the background sources and the sensor of the optical imaging system. In a worse situation, the object in the image could sometime be very faint relative to the background. Hence, a method to quantify noise models to a high precision is needed. For this purpose, an improved estimation of noise has been developed in [8].

Fig. 1.4a shows a region within the view of a telescope. Bright spots could be the objects of interest such as stars, man-made satellites, space debris etc. or an undesired cosmic ray trace while the grainy black and white spots are the background sources. These entities could be the result of the optical contaminations by air glow, scattered sunlight, moonlight and sensor's dark and read-out noise to mention a few. [12]. For the purpose of identifying, characterizing and tracking one or the other object under investigation we must ensure that these noises are taken into account and then a correct estimate is made.

Fig. 1.4b is the enlarged view of one of the bright spot. It is now clearly seen that the image is composed of pixelated data with each pixel corresponding to that of the sensor. These pixels have intensities proportional to the energy of the corresponding integrated photon counts incident on the pixel. A 3d bar chart is generated to show these pixel values on X-Y plane of a sensor (fig. 1.4c). The amount of photons counted depends in the intensity of the light, its wavelength and quantum efficiency of the detector. It is also proportional to the integration time, the time duration over

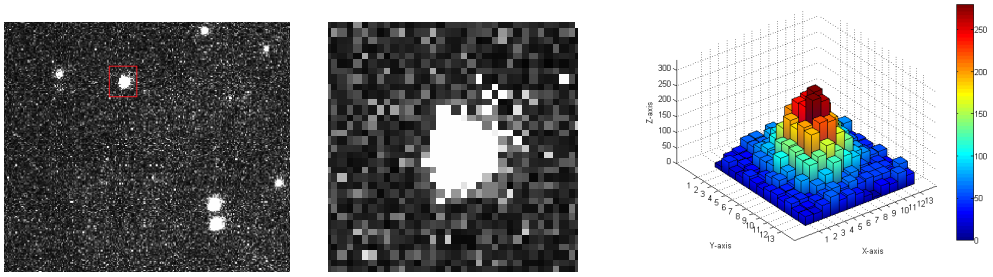

(a) (b) (c)

Figure 1.4. (a) Portion of the image obtained from a telescope (b) Enlarged view of the red square (c) 3d bar plot of the spot showing the relative intensities of light with respect to the background as detected by the sensor across 13×13 pixel frame

which the detector remains active. The actual photon count on all pixels is then given by the following [12]

$$C = \iint \frac{\pi}{4}(D-d)I(\overrightarrow{x},\lambda)\frac{\lambda}{hc}\mathrm{QE}(\lambda)e^{\tau(\lambda)\sec(\pi-\epsilon_{ele})}\mathrm{d}\lambda\mathrm{dt} \tag{1.1}$$

where $(D-d)$ is the effective aperture of the measuring device considering all obstructions, I the intensity of the source, QE the quantum efficiency of the detector and exponential function for atmospheric extinction. The counts are then converted into ADUs (Analog to Digital Units) for convenience by the image processor using suitable gain values.

$$ADU = \frac{C}{\text{gain}} \tag{1.2}$$

Throughout this work, we will use ADU in calculations and not the actual photon counts.

1.2.4 Signal-to-Noise Ratio (SNR) or the "CCD" equation

The signal to noise ratio (SNR) provide a feel of the quality of observation. The method to determine Signal-to-Noise Ratio (SNR) of the sensor image is given by using the "CCD" equation [13, 14]

$$\frac{S}{N} \simeq \frac{N_{total}}{\sqrt{N_{total} + n_{pix}\left(1 + \frac{n_{pix}}{n_B}\right)\left(N_{sky} + N_{digital} + N_{Readout}^2 + G^2\sigma_f^2\right)}} \tag{1.3}$$

where N_{total} is the total integrated signal measured, n_{pix} the number of pixels in the aperture, n_B the number of background only pixels, N_{sky} sky background variance, $N_{digital}$ digitization error variance, N_R the readout error variance and $G^2\sigma_f^2$ the uncertainty in estimating true mean of the distribution of fractional count per pixel. Equation 1.3 gives the SNR for the entire pixel array in consideration.

Equation 1.3 provides good theoretical information about the noise characteristics of the measurement data. Using the equation, one can determine whether the source is "faint" or "bright" since in bright source the SNR is dominated by the source itself ($\sqrt{N_{total}}$), whereas in the faint source other error terms are of equal or greater significance. [5] To improve the SNR of the image, it is noted in [14] that "the larger the number of background pixels selected, the better the correction for background and digitization and lower the noise." For individual pixel, equation1.3 becomes

$$\frac{S}{N} \simeq \frac{N_{total}}{\sqrt{N_{total} + \left(1 + \frac{1}{n_B}\right)\left(N_{sky} + N_{digital} + N_{Readout}^2 + G^2\sigma_f^2\right)}} \tag{1.4}$$

1.2.5 The Airy Pattern

Light from distant objects when incident on the aperture of the telescope optics is diffracted to form a bright central disc and a pattern of alternate bright and dark rings on the screen. They are known as the Airy disc and Airy diffraction pattern (named

after Airy who first wrote the theory behind it. [15]) respectively. The intensity of the diffraction pattern is mathematically expressed by the Bessel function

$$I(\theta) = I_0 \left(\frac{2J_1(kD\sin\theta)}{kD\sin\theta} \right)^2 \tag{1.5}$$

where D is the aperture radius, J_1 the Bessel function of first kind, $k = \frac{2\pi}{\lambda}$; λ is the wavelength of the light signal and θ is the angle of observation.

The Airy patterns are produced irrespective of the size of the relative aperture. [16] Each ring has a definite radius. For example, the distance between the center and the first minimum is given by

$$x = \arcsin\ (1.22\frac{\lambda f}{D}) \tag{1.6}$$

where f is the focal distance. Also, the total energy of the irradiance associated with the Airy pattern is given by [12, 17]

$$E = \int_0^\infty 2\pi I(\theta)\theta d\theta \tag{1.7}$$

It is found that the amount of energy in the central maximum is about 83.8% of the total.

When a CCD camera is used to image a distant object, light photons from the object is incident through the aperture on the detector array forming point source images. These point source object images are called as Point Spread Function (PSF).

1.2.6 The Point Spread Function (PSF)

Whenever the image of a point source is projected on an imaging sensor, it is not sharply resolved and the edges appear to have blurred. This blur is proportional to the amount of photons received by the sensor and depends on the distance from the source. This could also depend on the light collection angle and the medium between the aperture and the sensor. Such brightness distribution of the image on a sensor is known as Point Spread Function (PSF) [18]. Along with this, sources which have equal brightness distribution on all sides are called as Isotropic point sources.

Researchers have demonstrated that PSFs too have the form of Airy disc and pattern [19] (however, there can be effects of atmosphere on the Airy disc [12].) Defining PSFs as Airy discs makes mathematical calculations simple. Yet many investigators believe that Airy disc function is still tedious for calculations [12, 20]. Since most of the irradiation energy of the PSF is focused in the first maximum, it is well approximated by a Gaussian intensity function. Its general expression is given by eq. 1.8.

$$I = I_o \, \mathrm{e}^{-\frac{(x-\mu_x)^2 + (y-\mu_y)^2}{2\sigma^2}} \tag{1.8}$$

where I_o is the peak intensity at the centroid (μ_x, μ_y), I is the intensity at (x, y) and σ is the spread of the PSF (equal on all sides). The use of the Gaussian intensity function makes the calculation more tractable. Also, the approximation is valid for both microscopic as well as macroscopic point sources.

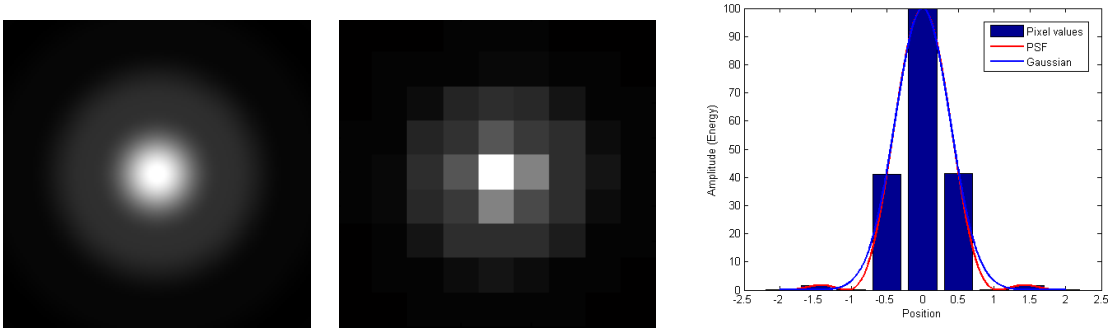

(a) (b) (c)

Figure 1.5. (a) An Airy disc (b) Pixelated image (c) Superposed plot of an approximated Gaussian model for the Airy disc

Fig. 1.5a shows a PSF generated by the Richard-Wolf [21] method (using ImageJ application [22]). Output from the CCD detectors are pixelated as in fig.1.5b. As a comparison, fig. 1.5c plots the approximated Gaussian model superposed over the Airy disc for some theoretical parameters [23].

2. STATE OF THE ART ALGORITHMS

Numerous algorithms exist that are able to determine parameters of a PSF such as the centroid, peak intensity at the centroid and the spread of the PSF. Some of the popular methods used in scientific applications for computing those parameters are the weighted center of gravity, least squares 2D optimization and the maximum likelihood estimation.

2.1 Iterative Weighted Center of Gravity

In this method, the centroid of the PSF is determined by calculating the first moment of the marginal distribution of the (x, y) count data. [24–26]

At first, the marginal distribution of the count data in each of the coordinate directions is formed. For the x coordinate, the marginal distribution is defined as the one-dimensional array of the sums of all counts along x coordinate for each y coordinate entry. Similarly, for the y coordinate it is defined as the one-dimensional array of the sums of all counts along y coordinate for each x coordinate entry. Mathematically, the marginal distribution in x and y coordinate directions are respectively given by

$$I_x = \sum_y I_{xy} \text{ and } I_y = \sum_x I_{xy} \tag{2.1}$$

where I_{xy} is the count of the pixel at (x, y).

As the next step, the first moment that is defined by the weighted mean is determined and is set equal to the centroid.

$$x_c = \frac{\sum_x I_x x}{\sum_x I_x}; y_c = \frac{\sum_y I_y y}{\sum_y I_y} \tag{2.2}$$

where (x, y) are the pixel coordinates.

This allows to obtain the centroid of the PSF. However, the accuracy of this

method suffers from high background noise. In order to improve the centroid accuracy in high background noise, eq. 2.2 is further weighted to take into account the shape of the spot. At the same time, to obtain better results when the initial estimates are far from the actual centroid, the centroiding process is iterated with updated weights [26]. The modified expression now becomes

$$(x_c(n), y_c(n)) = \left(\frac{\sum_x W_{xy}(n) I_x x}{\sum_x W_{xy}(n) I_x}, \frac{\sum_y W_{xy}(n) I_y y}{\sum_y W_{xy}(n) I_y} \right) \tag{2.3}$$

where $W_{xy}(n)$ is the weighting function given by the following Gaussian function.

$$W_{xy}(n) = a \cdot e^{-\left(\frac{(x - x_c(n-1))^2}{2\sigma_x^2} + \frac{(y - y_c(n-1))^2}{2\sigma_y^2} \right)} \tag{2.4}$$

a is set as the maximum intensity value from the array of count data I_{xy}. n is the number of iteration steps and σ_x and σ_y are obtained by approximating the FWHM of the PSF. FWHM is the width of the function where the intensity value is exactly half of the maximum (see chapter 6 for detail). In this method, the FWHM is found by taking the square root of the number of pixels which have intensity values higher than half of the maximum. σ_x and σ_y are then given by the equation

$$\sigma_x = \sigma_y = \frac{\text{FWHM}}{2\sqrt{2 \log 2}} \approx 0.4247 \times \text{FWHM} \tag{2.5}$$

The initial value for (x_b, y_b) is taken as the value of the brightest pixel in the entire measurement window. The iteration is performed until a certain threshold or maximum preset iteration count is reached. The iterative weighted center of gravity method has very high accuracy since the centroid is calculated empirically from the measurement data. However, the iterative procedure is very slow. The center of gravity method without iteration is also available and could be used in case the PSF is well formed and the initial centroid is not far from the true centroid.

2.2 Least Squares 2D Optimization

The Least squares 2D optimization method followed by [24] to determine centroid is based on minimizing the squared error function given by equation 2.6.

$$\min\ [\delta(\theta)] = \sum_{pixels} [V_{x,y} - f(x,y,\theta)]^2 \tag{2.6}$$

where $V_{x,y}$ is the measured intensity of the pixel at (x,y), $\theta = (a, x_b, y_b, \sigma_x, \sigma_y)$ is the vector containing parameters to be determined, and $f(x,y,\theta)$ is the function for the model PSF that is to be fitted using measured data. This function is defined as

$$f(x,y,\theta) \triangleq a \cdot e^{\frac{-(x-x_b)^2}{2\sigma_x^2}} e^{\frac{-(y-y_b)^2}{2\sigma_y^2}} \tag{2.7}$$

Basically, we try to minimize the squares of the error between the predicted model and the measurement data of the PSF. The initial estimate for θ is determined in the same way as in the center of gravity method. a is the magnitude of maximum intensity pixel, $(x_b,\ y_b)$ are chosen to be the coordinates of pixel with maximum intensity value and the $(\sigma_x,\ \sigma_y)$ are obtained by approximating the FWHM of the PSF. The final solution is then found by an iterative procedure using the Levenberg-Marquardt algorithm [24, 27]. The Levenberg-Marquardt (LM) technique is used to solve non-linear least square problems. This technique is a combination of two optimization methods: the gradient descent method and the Gauss-Newton method. The iterative procedure adaptively varies the algorithmic parameter updates between the gradient descent update and the Gauss-Newton update. The technique then approaches the Gauss-Newton method. Because of this, the LM algorithm provides a local minima and not a global minima. However, the algorithm gives a fairly accurate result since the initial estimate is chosen very near to the actual centroid.

In a different literature [20] a modified form of expression for weighted LS error criterion is given by

$$S = \sum_{pixels} \frac{(V_{x,y} - f(x,y,\theta))^2}{\nu} \tag{2.8}$$

where ν is the weight and is the expected variance of the signal in a particular pixel. This weight could vary depending on the type of signal, Poisson or Gaussian. Sometimes, when the mean number of photons per pixel is high, the Poisson noise can be approximated by the Gaussian noise (by the central limit theorem) [28].

2.3 Maximum Likelihood Estimation (MLE)

The maximum likelihood method [11, 29] to determine PSF parameters is based on forming a log-likelihood function of the parameter set $\boldsymbol{\theta} = (A, \bar{x}, \bar{y}, \sigma)$ given by 2.9 to calculate its gradient $\boldsymbol{\nabla}\ell$ and the Hessian matrix $\mathbf{H}$.

$$\ell(\boldsymbol{\theta}|g) = \ln \text{ pr}(g|\boldsymbol{\theta}) \tag{2.9}$$

Here A is the amplitude, $(\bar{x}, \bar{y})$ the centroid and σ the spread of the profile. Using these information, a nonlinear optimization routine is implemented to solve for $\boldsymbol{\theta}$ by increasing the likelihood using the equation

$$\boldsymbol{\theta}^{k+1} = \boldsymbol{\theta}^k - \left(\mathbf{H}^k\right)^{-1} \boldsymbol{\nabla} l^k \tag{2.10}$$

where k is the iteration index. $\mathbf{H}$ is evaluated at $\boldsymbol{\theta}^k$.

The Fisher information matrix $\mathbf{F}$ is formed in order to determine the accuracy of the estimates. $\mathbf{F}$ gives the covariance matrix $\mathbf{K}$ by the relation $\mathbf{K} = \mathbf{F}^{-1}$ calculated using the Cramér-Rao bound [11].[1] MLE has been theoretically shown to attain the maximum achievable precision (as an unbiased estimator) [30]. However, it is difficult to completely model the measured noise. Hence, there is always some bias in the estimation.

A detailed comparison among popular estimation techniques has been done in the work by Small et.al. [20]. Table 2.1 summarizes the differences between all the three types of methods discussed here along with the LS 2D analytical method developed in this work.

[1]Cramér-Rao bound (CRB) or Cramér-Rao lower bound (CRLB): According to the CRLB, the variance of any unbiased estimator is always greater than or equal to the inverse of the Fisher information. An estimator which is able to achieve this lower bound is called "efficient". Lower variance implies higher precision. Such an estimator is minimum variance unbiased (MVU) estimator.

Table 2.1. Summary and comparison of estimation techniques. First three methods are the state of the art algorithms while Iterative Weighted LS 2D analytical method is developed here

Criteria	**Iterative Weighted Center of gravity**	**Iterative LS 2D Optimization**	**Maximum Likelihood Estimator (MLE)**	**Iterative Weighted LS 2D Analytical Method (LS 2D AM)**	Advantages of LS 2D AM
Features of the method	• Uses empirical PSF data • Weighted average is found • Solution is determined numerically	• A model PSF is fitted optimally • Sum of LS error is minimized • Solution is determined numerically	• Parameters are found by increasing its log-likelihood using the measurement model • Solution is determined numerically • Estimator precision is known • Can achieve theoretical maximum precision	• A model PSF is fitted • Sum of LS errors of log function is minimized • Solution is determined analytically • Can perform almost as well as MLE at high photon counts	• Solution is determined analytically • No convergence issue
Assumptions	• Centroid is assumed to be near the initial estimate	• Centroid is assumed to be near the initial estimate • PSF is well formed	• Centroid is assumed to be close to the initial estimate • PSF is well formed • Noise is Gaussian or Poisson distributed • Requires that PSF and noise be carefully modeled	• PSF is well formed	• No assumption on initial centroid • Noise need not be explicitly modeled
Robustness against low intensity-low SNR pixels	Yes	No	Yes, robust against PSF width	Yes, robust against PSF shape (viz. Airy vs. Gaussian)	Robust, since shape is already approximated
Initial estimate required	Yes, need not be close	Yes	Yes	No	Initial estimate not needed
Accuracy	Accurate	Less accurate	Accurate	Accurate	Accurate estimation
Computation cost	High	High	High	Low	Low, due to preset number of iterations

3. PSF PARAMETER ESTIMATOR DEVELOPMENT

3.1 Overview

The least squares (LS) 2d analytical method developed in this work obtains the Gaussian approximation for the PSF. In the following section, some of the important assumptions are listed. Then the error functions for the least squares minimization are derived for two different cases. Finally, the analytical expressions for the Gaussian parameters are obtained.

3.2 Assumptions

Following are some of the assumptions in this development.

- **Unit width pixel** - Pixels are assumed to be square in shape with unit edge length. However, individual pixel dimensions does not matter as long as the measurement window size is available.
- **Closely packed mosaic** - CCD sensors are closely packed with no dead space in between pixels. In reality, detector have some space in between pixels because of constructional limitations of the silicon wafers.
- Each pixel in the detector produces a time integrated photon count. Analysis of the photoelectons at subpixel level is not done.
- All the calculations are done using ADU (Analog-Digital Unit) and not the actual photon count as ADU is convenient to work with. Also, the CCD gain value is known.

3.3 Iterative Weighted LS 2D Error Function

In this work, the PSF intensity is fitted with a two dimensional Gaussian distribution. The method is based on the previous work for one dimensional distribution by Hongwei [31]. Hongwei's method works by minimizing the sum of the least squares of the errors between the logarithm of the measured intensities and the logarithm of a model Gaussian Intensity function in one dimension. Here, the work is extended to two dimensional distributions.

At first, a bivariate Gaussian intensity function with uncorrelated width along the pixel edges is defined. It is given by equation 3.1.

$$Z = Z_o e^{-\frac{(x-u_x)^2}{2\sigma_x^2} - \frac{(y-u_y)^2}{2\sigma_y^2}} \tag{3.1}$$

where u_x, u_y = Centroid on (x, y) plane

Z_o = peak intensity at the centroid

σ_x, σ_y = standard deviation or spread along x and y axes

Taking natural logarithm on both sides

$$\begin{aligned} \ln Z &= \ln Z_o - \left(\frac{x^2 + u_x^2 - 2xu_x}{2\sigma_x^2} + \frac{y^2 + u_y^2 - 2yu_y}{2\sigma_y^2} \right) \\ &= \ln Z_o - \frac{u_x^2}{2\sigma_x^2} - \frac{u_y^2}{2\sigma_y^2} + \frac{2xu_x}{2\sigma_x^2} - \frac{x^2}{2\sigma_x^2} + \frac{2yu_y}{2\sigma_y^2} - \frac{y^2}{2\sigma_y^2} \end{aligned} \tag{3.2}$$

Rewriting above as

$$\ln Z = a + bx + cx^2 + py + qy^2 \tag{3.3}$$

$$\text{where } a = \ln Z_o - \frac{u_x^2}{2\sigma_x^2} - \frac{u_y^2}{2\sigma_y^2}$$

$$b = \frac{2u_x}{2\sigma_x^2}, \quad c = \frac{-1}{2\sigma_x^2}$$

$$p = \frac{2u_y}{2\sigma_y^2}, \quad q = \frac{-1}{2\sigma_y^2}$$

The error function for LS minimization is defined as

$$\delta = \ln Z - \left(a + bx + cx^2 + py + qy^2\right) \tag{3.4}$$

Now, if the zero mean additive noise in the measurement is given by η, we can say that

$$\hat{Z} = Z + \eta \tag{3.5}$$

where $\hat{Z}$ is the PSF data.
The error function is redefined as

$$\hat{\delta} = \ln \hat{Z} - (a + bx + cx^2 + py + qy^2) \tag{3.6}$$

Expanding this $\hat{\delta}$ by Taylor-Maclaurin expansion up to second order, we have

$$\hat{\delta} = \ln (Z + \eta) - \left(a + bx + cx^2 + py + qy^2\right) \tag{3.7}$$

$$= \ln Z - \left(a + bx + cx^2 + py + qy^2\right) + \frac{\eta}{Z} - \frac{1}{2}\left(\frac{\eta}{Z}\right)^2 + \ldots (HOT) \tag{3.8}$$

Reasonably neglecting second and higher order terms of η in equation 3.8 and taking the expectation of $\hat{\delta}^2$, we get

$$\mathrm{E}[\hat{\delta}^2] = \left[\ln (Z) - \left(a + bx + cx^2 + py + qy^2\right)\right]^2 + \frac{\sigma_\eta^2}{Z^2} \tag{3.9}$$

where σ_η^2 is the noise variance. Since the Gaussian PSF decays very rapidly, the low intensity pixels near the tail could have a large impact on the estimates [20]. The presence of Z^2 in the denominator means it could cause the estimator to become highly sensitive to noises especially those in the low intensity-low SNR region near the tail of the PSF while being nominal on the brighter pixels close to the centroid. Discarding the low intensity data on the other hand could result into loss of meaningful PSF information.

One of the way of getting around the issue is by multiply the error function in equation 3.8 by the weighting factor $\hat{Z}$. The weighted error function now becomes

$$\varepsilon = \hat{Z}\hat{\delta} \tag{3.10}$$

$$= \hat{Z}\left[\ln \hat{Z} - \left(a + bx + cx^2 + py + qy^2\right)\right] \tag{3.11}$$

$$\varepsilon \approx \hat{Z}\left[\ln\left(Z\right) - \left(a + bx + cx^2 + py + qy^2\right)\right] + \eta \tag{3.12}$$

The expectation of ε^2 is now

$$\mathrm{E}[\varepsilon^2] = \hat{Z}^2\left[\ln\left(Z\right) - \left(a + bx + cx^2 + py + qy^2\right)\right]^2 + \sigma_\eta^2 \tag{3.13}$$

This way, we can minimize the variations of the sensitivity of the estimator across low to high SNR regions. Figure 3.1 shows the effect of weight factor on the estimate.

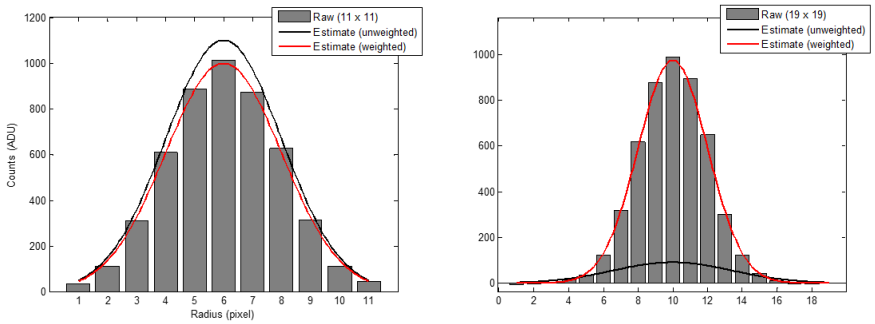

(a) 11×11 (b) 19×19

Figure 3.1. 2D section showing the effect of weight factor on peak estimates for 11×11 and 19×19 observation frames. Former has fewer background dominated pixels whereas latter has many, thus leading to over and underestimation. (Given paramters: $Z_o = 1000$ ADU, $U_x = 6px, \sigma = 2px$, sky =100 ADU, readout = 10 ADU)

Using equation 3.11 the sum of squared error across $N_1 \times N_2$ pixel window is found, given by equation 3.14.

$$\varepsilon^2_{N_1 \times N_2} = \sum_{N_1}\sum_{N^2} \hat{Z}^2\left[\ln\,\hat{Z} - \left(a + bx + cx^2 + py + qy^2\right)\right]^2 \tag{3.14}$$

The least squares minimization of equation 3.14 implies estimating variables a, b, c, p and q. On differentiating this equation with respect to a, b, c, p and q and setting the resultant equal to 0 we get the following system of equations.

$$\begin{bmatrix} \sum \hat{Z}^2 & \sum x\hat{Z}^2 & \sum x^2\hat{Z}^2 & \sum y\hat{Z}^2 & \sum y^2\hat{Z}^2 \\ \sum x\hat{Z}^2 & \sum x^2\hat{Z}^2 & \sum x^3\hat{Z}^2 & \sum xy\hat{Z}^2 & \sum xy^2\hat{Z}^2 \\ \sum x^2\hat{Z}^2 & \sum x^3\hat{Z}^2 & \sum x^4\hat{Z}^2 & \sum x^2y\hat{Z}^2 & \sum x^2y^2\hat{Z}^2 \\ \sum y\hat{Z}^2 & \sum xy\hat{Z}^2 & \sum x^2y\hat{Z}^2 & \sum y^2\hat{Z}^2 & \sum y^3\hat{Z}^2 \\ \sum y^2\hat{Z}^2 & \sum xy^2\hat{Z}^2 & \sum x^2y^2\hat{Z}^2 & \sum y^3\hat{Z}^2 & \sum y^4\hat{Z}^2 \end{bmatrix} \begin{bmatrix} a \\ b \\ c \\ p \\ q \end{bmatrix} = \begin{bmatrix} \sum \hat{Z}^2\ln(\hat{Z}) \\ \sum x\hat{Z}^2\ln(\hat{Z}) \\ \sum x^2\hat{Z}^2\ln(\hat{Z}) \\ \sum y\hat{Z}^2\ln(\hat{Z}) \\ \sum y^2\hat{Z}^2\ln(\hat{Z}) \end{bmatrix} \tag{3.15}$$

One thing to note, since we omitted the higher order terms of the Taylor expansion in equation 3.8, the noise is now described inadequately due to the bias in the measurement model. Moreover, this is prominent in the low intensity regions. To minimize the bias introduced earlier in the approximation we will iterate equation 3.15 with updated weight $\hat{Z}_k$ at each iteration. The idea is to eventually decrease the difference between $\hat{Z}$ and Z. The system of equations for iterative procedure is given by

$$\begin{bmatrix} \sum Z_k^2 & \sum xZ_k^2 & \sum x^2Z_k^2 & \sum yZ_k^2 & \sum y^2Z_k^2 \\ \sum xZ_k^2 & \sum x^2Z_k^2 & \sum x^3Z_k^2 & \sum xyZ_k^2 & \sum xy^2Z_k^2 \\ \sum x^2Z_k^2 & \sum x^3Z_k^2 & \sum x^4Z_k^2 & \sum x^2yZ_k^2 & \sum x^2y^2Z_k^2 \\ \sum yZ_k^2 & \sum xyZ_k^2 & \sum x^2yZ_k^2 & \sum y^2Z_k^2 & \sum y^3Z_k^2 \\ \sum y^2Z_k^2 & \sum xy^2Z_k^2 & \sum x^2y^2Z_k^2 & \sum y^3Z_k^2 & \sum y^4Z_k^2 \end{bmatrix} \begin{bmatrix} a \\ b \\ c \\ p \\ q \end{bmatrix} = \begin{bmatrix} \sum Z_k^2\ln(\hat{Z}) \\ \sum xZ_k^2\ln(\hat{Z}) \\ \sum x^2Z_k^2\ln(\hat{Z}) \\ \sum yZ_k^2\ln(\hat{Z}) \\ \sum y^2Z_k^2\ln(\hat{Z}) \end{bmatrix} \tag{3.16}$$

where

$$Z_k = \begin{cases} \hat{Z} & \text{when } k = 0 \\ e^{a_{(k)}+b_{(k)}x+c_{(k)}x^2+p_{(k)}y+q_{(k)}y^2} & \text{when } k > 0 \end{cases} \tag{3.17}$$

Iterative 2d weighted LS Gaussian approximation for non-aligned elliptically spread sources

The method explained above corresponds to the Gaussian approximation for elliptically spread sources whose major and minor axes are assumed to be along the edges of a typical square detector pixel. In reality, images are generally non-aligned to the pixel axes. Fig. 3.2a shows a linearly scaled light source entity in a flattened image obtained from the telescope. Fig. 3.2b on the right is the contour plot of the intensity on x-y plane. The third, fig. 3.2c is the contour of the profile approximated by simulating this image over 6 iterations using the algorithm described above. The values

of the parameters obtained after these many iterations are $Z_o = 17254.616$ ADUs, $u_x = 13.951\text{px}, u_y = 17.284\text{px}, \sigma_x = 2.097$ and $\sigma_y = 2.68$. The known maximum intensity of this image is about 19500 ADUs as found from the image processing software *SAOImage DS9* [32]. Hence the approximated peak is nearly 88.48% of actual maximum.

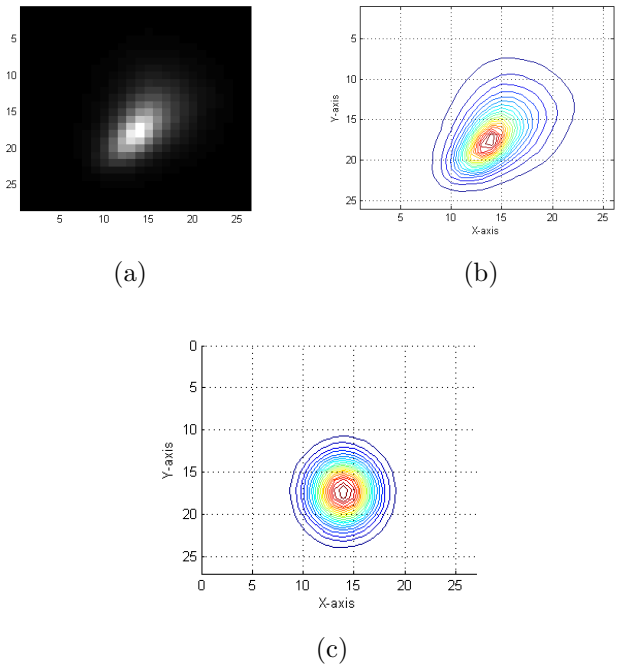

Figure 3.2. (a) An elliptical light source with major and minor axes non-aligned to the co-ordinate axes (b) Representation of the image using contours of the intensities (c) Contour of the approximated profile showing obvious deviation from actual shape when σ_x and σ_y are assumed to be uncorrelated

The algorithm clearly fails to achieve the profile shape of the source. This is mostly because σ_x and σ_y which were initially stated as uncorrelated are in general correlated to each other. In celestial images, not all objects are aligned to horizontal or vertical axes. Some of them have certain rotation from the axes. In that case, it is important to take into account their orientations before the estimation is made.

Correlation (given by ρ) defines the orientation of the Gaussian. Hence it must be incorporated in the system of equations in order to minimize the difference between the actual and approximated profiles. The method described earlier can still be used in case the approximation is to be limited to the aligned state only.

In order to include the correlation information in the algorithm we incorporate covariance matrix with the possibility of the presence of cross covariance terms in it. The initial formula for the intensity function given by equation 3.1 is now more generalized as

$$Z = Z_o e^{\{-\frac{1}{2}(X-U)^T \Sigma^{-1}(X-U)\}} \tag{3.18}$$

where X is the position vector of the local frame in pixels, U is the mean position (or the centroid estimate) and Σ is the covariance matrix of the function.
Working on equation 3.18 by expanding the terms,

$$\begin{aligned}
Z &= Z_o e^{\left\{-\frac{1}{2}\left(\begin{bmatrix}x\\y\end{bmatrix}-\begin{bmatrix}u_x\\u_y\end{bmatrix}\right)^T \begin{bmatrix}\sigma_x^2 & \rho\sigma_x\sigma_y\\ \rho\sigma_x\sigma_y & \sigma_y^2\end{bmatrix}^{-1}\left(\begin{bmatrix}x\\y\end{bmatrix}-\begin{bmatrix}u_x\\u_y\end{bmatrix}\right)\right\}} \\
&= Z_o e^{\left\{-\frac{(x-u_x)^2}{2\sigma_x^2(1-\rho^2)}-\frac{(y-u_y)^2}{2\sigma_y^2(1-\rho^2)}+\frac{(x-u_x)(y-u_y)\rho}{\sigma_x\sigma_y(1-\rho^2)}\right\}} \\
&= Z_o e^{\left\{-\frac{x^2}{2\sigma_x^2(1-\rho^2)}-\frac{y^2}{2\sigma_y^2(1-\rho^2)}+\frac{xy\rho}{\sigma_x\sigma_y(1-\rho^2)}+\frac{xu_x}{\sigma_x^2(1-\rho^2)}-\frac{xu_y\rho}{\sigma_x\sigma_y(1-\rho^2)}\right.} \\
&\qquad \left.+\frac{yu_y}{\sigma_y^2(1-\rho^2)}-\frac{yu_x\rho}{\sigma_x\sigma_y(1-\rho^2)}-\frac{u_x^2}{2\sigma_x^2(1-\rho^2)}-\frac{u_y^2}{2\sigma_y^2(1-\rho^2)}+\frac{u_xu_y\rho}{\sigma_x\sigma_y(1-\rho^2)}\right\}
\end{aligned}$$

Taking natural logarithm on both sides

$$\begin{aligned}
\ln Z = \ln Z_o + \Bigg\{ &-\frac{x^2}{2\sigma_x^2(1-\rho^2)}-\frac{y^2}{2\sigma_y^2(1-\rho^2)}+\frac{xy\rho}{\sigma_x\sigma_y(1-\rho^2)}+\frac{xu_x}{\sigma_x^2(1-\rho^2)}-\frac{xu_y\rho}{\sigma_x\sigma_y(1-\rho^2)} \\
&+\frac{yu_y}{\sigma_y^2(1-\rho^2)}-\frac{yu_x\rho}{\sigma_x\sigma_y(1-\rho^2)}-\frac{u_x^2}{2\sigma_x^2(1-\rho^2)}-\frac{u_y^2}{2\sigma_y^2(1-\rho^2)}+\frac{u_xu_y\rho}{\sigma_x\sigma_y(1-\rho^2)}\Bigg\}
\end{aligned}$$

$$\text{Let } a = \ln Z_o - \frac{u_x^2}{2\sigma_x^2(1-\rho^2)} - \frac{u_y^2}{2\sigma_y^2(1-\rho^2)} + \frac{u_x u_y \rho}{\sigma_x \sigma_y (1-\rho^2)} \tag{3.19}$$

$$b = \frac{u_x}{\sigma_x^2(1-\rho^2)} - \frac{u_y \rho}{\sigma_x \sigma_y (1-\rho^2)};\ c = \frac{1}{2\sigma_x^2(1-\rho^2)} \tag{3.20}$$

$$p = \frac{y u_y}{\sigma_y^2(1-\rho^2)} - \frac{y u_x \rho}{\sigma_x \sigma_y (1-\rho^2)};\ q = \frac{1}{2\sigma_y^2(1-\rho^2)} \tag{3.21}$$

$$d = \frac{\rho}{\sigma_x \sigma_y (1-\rho^2)} \tag{3.22}$$

We get

$$\ln Z = a + bx + cx^2 + py + qy^2 + dxy \tag{3.23}$$

If the zero mean additive noise in the measurement is given by η, then $\hat{Z} = Z + \eta$.

Following similar procedure as explained in equations 3.8 to 3.14, we obtain for each pixel

$$\varepsilon^2 = \hat{Z}^2 \left[\ln \hat{Z} - \left(a + bx + cx^2 + py + qy^2 + dxy\right)\right]^2 \tag{3.24}$$

$$\begin{aligned} &= \hat{Z}^2 \Big[(\ln \hat{Z})^2 + \left(a + bx + cx^2 + py + qy^2 + dxy\right)^2 \\ &\qquad - 2 \ln \hat{Z} \left(a + bx + cx^2 + py + qy^2 + dxy\right)\Big] \end{aligned} \tag{3.25}$$

Partial differentiating equation 3.25 with respect to a and equating it to 0

$$\frac{\partial \varepsilon^2}{\partial a} = \hat{Z}^2 \left[2\left(a + bx + cx^2 + py + qy^2 + dxy\right) - 2 \ln \hat{Z}\right] = 0 \tag{3.26}$$

Similarly, differentiating partially with respect to other parameters b, c, p, q, d and equating each to 0, we obtain the system of equations

$$\hat{Z}^2 \begin{bmatrix} (a + bx + cx^2 + py + qy^2 + dxy) - \ln \hat{Z} \\ x\,(a + bx + cx^2 + py + qy^2 + dxy) - \ln \hat{Z} \\ x^2\,(a + bx + cx^2 + py + qy^2 + dxy) - \ln \hat{Z} \\ y\,(a + bx + cx^2 + py + qy^2 + dxy) - \ln \hat{Z} \\ y^2\,(a + bx + cx^2 + py + qy^2 + dxy) - \ln \hat{Z} \\ xy\,(a + bx + cx^2 + py + qy^2 + dxy) - \ln \hat{Z} \end{bmatrix} = 0 \tag{3.27}$$

The outer $\hat{Z}^2$ forms the weight for the equation and is updated with a new value given by $\hat{Z}_k^2$ after every iteration. Summing over all the pixels and rearranging equation 3.27 to the matrix form ,

$$\begin{bmatrix} \sum Z_k^2 & \sum xZ_k^2 & \sum x^2Z_k^2 & \sum yZ_k^2 & \sum y^2Z_k^2 & \sum xyZ_k^2 \\ \sum xZ_k^2 & \sum x^2Z_k^2 & \sum x^3Z_k^2 & \sum xyZ_k^2 & \sum xy^2Z_k^2 & \sum x^2yZ_k^2 \\ \sum x^2Z_k^2 & \sum x^3Z_k^2 & \sum x^4Z_k^2 & \sum x^2yZ_k^2 & \sum x^2y^2Z_k^2 & \sum x^3yZ_k^2 \\ \sum yZ_k^2 & \sum xyZ_k^2 & \sum x^2yZ_k^2 & \sum y^2Z_k^2 & \sum y^3Z_k^2 & \sum xy^2Z_k^2 \\ \sum y^2Z_k^2 & \sum xy^2Z_k^2 & \sum x^2y^2Z_k^2 & \sum y^3Z_k^2 & \sum y^4Z_k^2 & \sum xy^3Z_k^2 \\ \sum xyZ_k^2 & \sum x^2yZ_k^2 & \sum x^3yZ_k^2 & \sum xy^2Z_k^2 & \sum xy^3Z_k^2 & \sum x^2y^2Z_k^2 \end{bmatrix} \begin{bmatrix} a \\ b \\ c \\ p \\ q \\ d \end{bmatrix} = \begin{bmatrix} \sum Z_k^2 \ln(\hat{Z}) \\ \sum xZ_k^2 \ln(\hat{Z}) \\ \sum x^2Z_k^2 \ln(\hat{Z}) \\ \sum yZ_k^2 \ln(\hat{Z}) \\ \sum y^2Z_k^2 \ln(\hat{Z}) \\ \sum xyZ_k^2 \ln(\hat{Z}) \end{bmatrix} \tag{3.28}$$

where Z_k is the weight for k^{th} iteration given by

$$Z_k = \begin{cases} \hat{Z} & \text{when } k = 0 \\ e^{a_{(k)} + b_{(k)}x + c_{(k)}x^2 + p_{(k)}y + q_{(k)}y^2 + d_{(k)}xy} & \text{when } k > 0 \end{cases} \tag{3.29}$$

$\sum$ represents the sum over all the pixels i.e. $\sum_{N_1} \sum_{N_2}$ where N_1 and N_2 are the dimensions (in pixels) on the detector plane in the measurement window. Note that the $\hat{Z}$ term in the logarithm on the right hand side of equation 3.28 remains constant throughout the iteration process.

Once the iterations are completed and the parameters a, b, c, p, q and d are found, values for the Gaussian PSF variables $u_x, u_y, \sigma_x, \sigma_y, \rho$ and Z_o are determined by substitutions.

3.4 Parameter Estimation

From the estimates of a, b, c, p, q and d, the Gaussian parameters are obtained simply by reversing equation 3.23.

3.4.1 Correlation coefficient

Correlation coefficient, ρ is obtained first since other parameters depend on this value. From equation 3.22

$$\rho = d\left\{\sigma_x \sigma_y (1 - \rho^2)\right\}$$

Squaring both sides,

$$\rho^2 = d^2 \left\{\sigma_x^2 \sigma_y^2 (1-\rho^2)^2\right\} = \frac{d^2}{1/\left\{\sigma_x^2 \sigma_y^2 (1-\rho^2)^2\right\}}$$

Substituting c and q from equations 3.20 and 3.21, $\rho^2 = \dfrac{d^2}{4cq}$. where $-1 < \rho < 1$

The actual value of ρ has to be found in conjunction with the peak magnitude Z_o since we do not know whether ρ is negative or positive at this point. It is noticed that using ρ as the negative of the actual value does not give an optimum value of Z_o. Furthermore, in crowded fields Z_o is established using the sharpness and roundness criteria, making the result more optimum.

3.4.2 Sub-pixel Centroid

Similar to the correlation coefficient, the sub-pixel centroid (u_x, u_y) is obtained from the estimates of a, b, c, p, q and r and is given by equation 3.30

$$U = (u_x, u_y) = \left[\frac{\left(\dfrac{dp}{2q} - b\right)}{\left(2c - \dfrac{d^2}{2q}\right)}, \frac{\left(\dfrac{db}{2c} - p\right)}{\left(2q - \dfrac{d^2}{2c}\right)} \right] \tag{3.30}$$

This gives the centroid of the PSF in the local frame window. To obtain centroid of a particular source in the image, proper co-ordinate adjustment must be done, like adding the relative coordinate location of the local frame in the image.

3.4.3 Standard Deviation or the Spread (σ_x, σ_y)

The standard deviation or the width of the PSF is given by

$$\sigma = (\sigma_x, \sigma_y) = \left(\sqrt{\frac{-1}{2c(1-\rho^2)}}, \sqrt{\frac{-1}{2q(1-\rho^2)}} \right) \tag{3.31}$$

These values are always positive.

3.4.4 Peak Magnitude

The magnitude of the peak at the centroid is determined from equation 3.32

$$Z_o = e^{\left(a + \dfrac{u_x^2}{2\sigma_x^2(1-\rho^2)} + \dfrac{u_y^2}{2\sigma_y^2(1-\rho^2)} - \dfrac{\rho u_x u_y}{\sigma_x \sigma_y (1-\rho^2)} \right)} \tag{3.32}$$

where parameters have usual meaning. As noted previously, for crowded-field photometry Z_o is passed through the sharpness and the roundness criteria which eventually establishes whether the source is a PSF or an erroneous data from bad pixels or cosmic ray events.

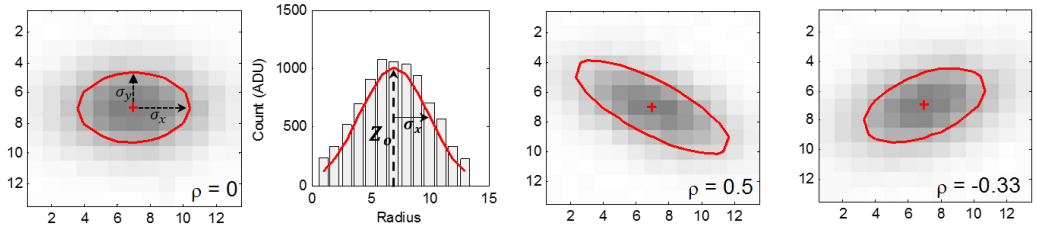

Figure 3.3. Physical significance of the estimated Gaussian parameters. From left to right, σ represents the spread or half width, Z_o the peak count, U the centroid or the location of the peak and ρ determines the shape of the profile as shown in the last two images.

4. SIMULATION

Simulations are done to obtain Gaussian approximations of the PSF using the system of equations developed in section 3.3. Initially a symmetric point source is simulated. Subsequent simulations are performed on asymmetric and non-aligned profiles to determine centroid and other parameters. For each of the scenarios two test cases of low and high SNR are formed.

4.1 Image Construction

As discussed in chapter 1, locating an object of interest in a celestial image is important for the identification and cataloging of the object. It is therefore necessary to obtain the centroid of the object's image (as well as that of the nearby stars) with a high precision. Artificial images are generated to simulate such celestial images. This enable us to understand the effectiveness of the centroiding algorithm. At the same time other parameters of the object are also found. In order to achieve a better indication, the image generation process should allow for including both the celestial as well as the sensor noise to the image.

At first, a Gaussian intensity distribution resembling a PSF is formed with the predefined parameters for an $N \times N$ detector window. Then each of the pixel values are replaced by a value from Poisson distribution about that intensity. Once all the pixel values are replaced by the corresponding Poisson distributed intensities, a constant background (which vary according to Poisson statistics as well) is added to the data along with Gaussian distributed readout noise. This simulated image is then tested with the developed algorithm. Fig. 4.1 shows the break-up of the counts in a typical raw image of the PSF from the detector. In this image, the source has a peak of 125 ADU, sky is Poisson distributed about 100 ADU and the sensor readout has an uncertainty of about 10 ADU. Note that ADU in each pixel represents integrated

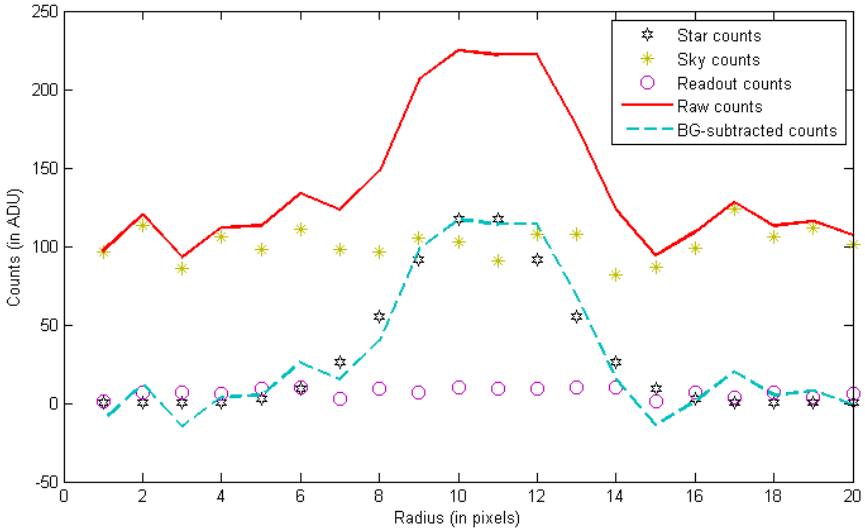

Figure 4.1. Construction of the raw image of a PSF. Markers show the individual signal counts while solid and dotted lines show the raw and background subtracted counts for PSF approximation. Total signal available as detector output is the sum of markers count in every pixel.

photometric signal of that pixel. (Actual addition of all sources is done at electron level in a real instrument [33].)

4.1.1 Symmetric PSF

A symmetric point source is constructed using arbitrary values of the parameters where

$$[Z_o = 10000 \text{ ADU}, u_x = 10.5px, u_y = 10.5px, \sigma = 2 \text{ pixels}]$$

Added to it is a randomly varying sky background with the mean and variance of 100 ADU. The image is corrupted by an additive white noise (as readout) of 10 ADU. The local detector window size is set as 20×20 pixel^2. From the CCD equation, the signal to noise ratio (SNR) of the constructed image is found to be about 15. This

scenario is equivalent to imaging a 13^{th} magnitude[1] celestial object (for a CCD with zero point of the scale = 25 and gain = $1e^{-}$/ADU) with telescope in a non-polluted night sky. In another case, the source now has the peak intensity of 125 ADU, while other parameters are kept the same. This source is equivalent to one 18^{th} magnitude celestial object (star, satellite etc.) and has SNR = 0.75.

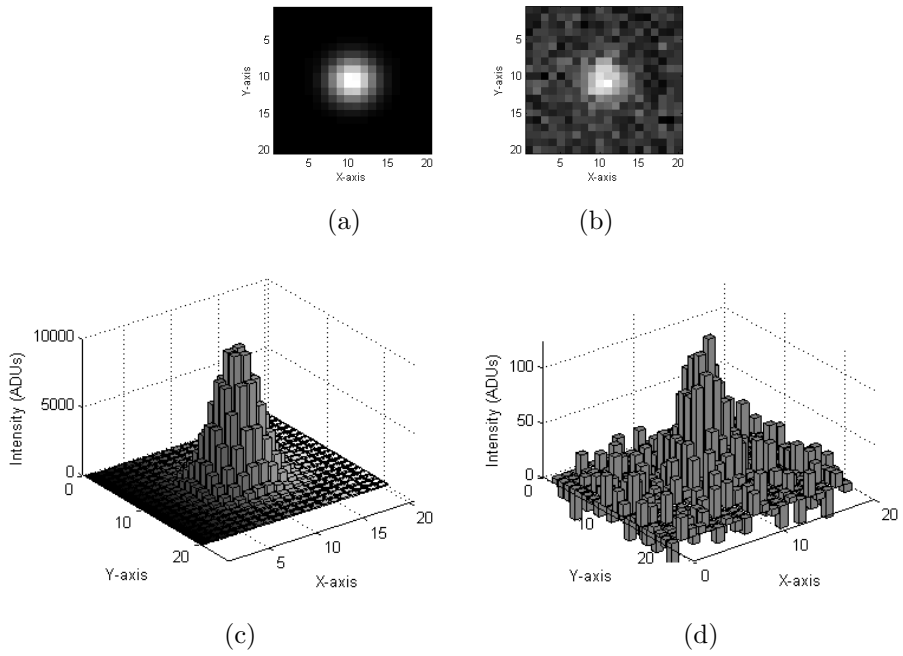

Figure 4.2. Artificial PSFs as simulated for detected source with corresponding 3d bar plot right below the image. Each bar depicts the brightness value of that pixel above background level. Centroid is at (10.5, 10.5) and SNR is 15 and 0.75 respectively. Note that sources are fully contained in the measurement frame.

Fig. 4.2 shows the plot of the intensities of the two point sources. In fig. 4.2a and 4.2b, numbers along horizontal and vertical axes indicate grid of the detector window.

[1]Magnitude of celestial object: It is a number that describes the brightness of a celestial object as seen from Earth. It is function of negative logarithm. For a given wavelength, it is obtained from the equation: $m - m_o = -2.5\log_{10}\left(\frac{F}{F_o}\right)$, where m is the apparent magnitude, F the luminous intensity of the object, m_o the reference magnitude and F_o the luminous intensity of the reference object. An increase in the apparent magnitude is therefore a decrease in the brightness of the object.

Simulation is done and result estimated from 5000 sample runs. Values of the parameters for fig. 4.2a are found as

$$[Z_o = 10059, u_x = 10.5001px, u_y = 10.5px, \sigma = 1.996 \text{ pixels}]$$

where as for the fig. 4.2b the values are

$$[Z_o = 120.9996, u_x = 10.5006px, u_y = 10.4994px \text{ and } \sigma = 2.1086 \text{ pixels}]$$

In both the cases, estimates for the centroid were over 99.99% accurate. Accuracy of the peak for high SNR source was about 99.4% and that for the low SNR source, it was about 96.8%. Units for Z_o and σ are ADU unless otherwise mentioned.

4.1.2 Asymmetric and Non-Aligned Profiles

The test case for asymmetric PSF is similar to that of symmetric with the only variation in the standard deviation or the spread of the distribution σ_x and σ_y. Here the point source is constructed with the uncorrelated $\sigma_x = 2$ and $\sigma_y = 4$ while keeping rest of the parameter same as the symmetric source in section 4.1.1. Adding randomly varying sky background with the mean and variance of 100 ADU produce images of SNR = 25 and 1.4 respectively. Fig. 4.3a and 4.3b are the two cases of the defined asymmetric source.

To simulate a non-aligned source with a peak of 125 ADU, the correlation term is incorporated in the calculation (equation 3.18). Hence, the standard deviations σ_x and σ_y are no longer uncorrelated. The covariance matrix for the non-aligned case is set as $\Sigma = \begin{pmatrix} 4 & -2 \\ -2 & 16 \end{pmatrix}$ where $\rho = -0.25$. Fig. 4.3c shows the simulated non-aligned source.

Results are estimated from a sample of 5000 simulation runs. For image 4.3a, parameters obtained are

$$[Z_o = 10021, u_x = 10.5px, u_y = 10.5px, \sigma_x = 1.9983 \text{ px and } \sigma_y = 3.9974 \text{ px}]$$

For the image 4.3b,

$$[Z_o = 126.844, u_x = 10.4996px, u_y = 10.5016px, \sigma_x = 1.9331 \text{ px and } \sigma_y = 3.8293 \text{ px}]$$

Similarly for the non-aligned source 4.3c,

$$[Z_o = 124.3941, u_x = 10.4973px, u_y = 10.5064px, \sigma_x = 1.9356 \text{ px}, \sigma_y = 3.8423 \text{ px, and } \rho = -0.247]$$

Units are ADU unless otherwise mentioned. Estimates for the centroid in all three cases were over 99.9% accurate. On the other hand, peak estimates were about 99.8%, 98.5% and 99.5% accurate respectively, indicating the high accuracy of the algorithm.

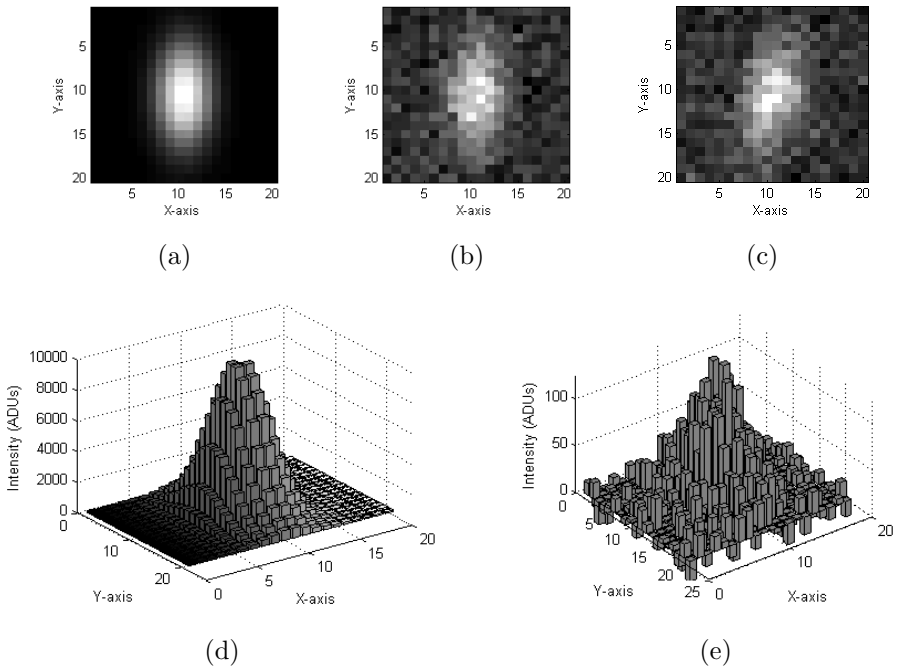

Figure 4.3. Artificially generated images for detected asymmetric point sources. The corresponding bar plot for (a) and (b) below the images shows background subtracted intensities of pixels. Centroid in both the case is at (10.5, 10.5), $\sigma_x = 2, \sigma_y = 4$ and SNR of 25 and 1.4 respectively (c) A non-aligned source with SNR = 1.37

Table 4.1. Summary of the results for the three scenarios

Scenario	SNR	Z_o error (%)	Centroid error (px)
Symmetric	15	0.59	0.0001
	0.75	3.2	0.0008
Asymmetric	25	0.21	≈0
	1.4	1.48	0.0016
Asymmetric Non-aligned	1.37	0.48	0.007

4.2 Results

4.2.1 Estimation Residual

One of the main purpose of iteration in the estimation procedure is to reduce the estimate error brought in by the bias in the measurement model. Fig. 4.4 plots the effect of iteration on the estimation residual (the difference between the estimate after the iteration and the observed peak). The parameters used are those of the 15 to 20^{th} magnitude objects with the noise data as explained in section 4.1.1. As the

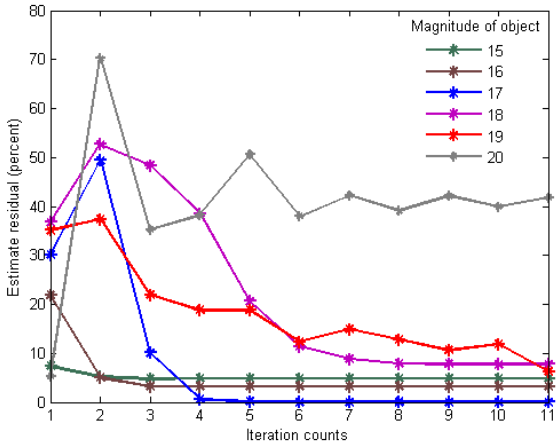

Figure 4.4. Percentage residual of peak estimates with respect to number of iterations

iteration count increases, the difference between the estimate and the observed data becomes lesser and hence the residual decreases. Notice that the estimate has the

best result after 8 iterations for up to 19^{th} magnitude object. For a very faint object of 20^{th} magnitude, the estimate has a very large residual.

It must be noted that the residual does not necessarily represent the accuracy of the estimate. This is so because the peak in the observed data is generally contaminated with randomly varying noises. Sources having low pixel counts (as in the 20^{th} magnitude object) are prone to higher contaminations. At the same time, it is possible that the observed peaks are not the same as the true peaks of the PSF due to the discrete nature of the pixel data.

4.2.2 Accuracy

Several simulations were run in order to predict the performance of the algorithm. During the simulations, the noise level was varied from low to high and the corresponding error in the estimate plotted. Though this analysis is done on the symmetric PSFs, similar result can be shown on asymmetric as well as asymmetric non-aligned sources.

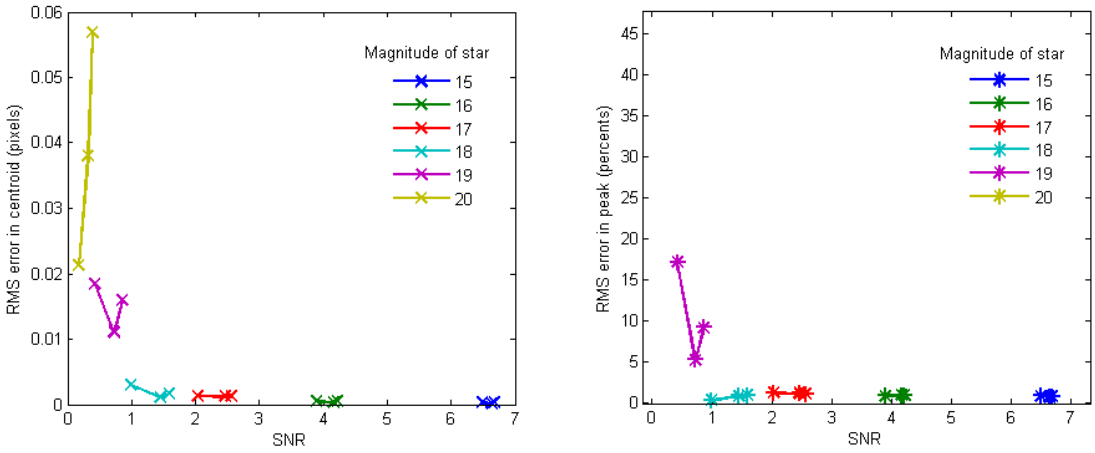

(a) RMS error in the centroid (in pixels)

(b) % RMS error in the peak estimate

Figure 4.5. Plot of RMS error in the estimates for images with different magnitudes, each at three levels of background 0, 10 and 50 ADU. The diagram can be well used to understand the variation of RMS error with varying magnitude.

Fig. 4.5a shows the plot of the rms error in the centroid with respect to the SNRs for the sources of different magnitudes, while fig. 4.5b shows the plot of the percentage rms error in the peak with respect to the SNRs for the corresponding sources.

Upon observation, the RMS error in the peak is found to be less than 2% up to the source (star) of magnitude 18. The error increases rapidly as source becomes fainter. This occurs especially when SNR falls under 1. On the other hand, by carefully observing the RMS error in the centroid, we can say that even for a faintest source of magnitude 20, the error is found to be less than one-tenth of the pixel. For brighter ones the accuracy is much higher in order of one-hundredth of a pixel which is a fair estimation using noisy data. Hence, even though the peak estimate is accurate for the sources only up to 18^{th} magnitude, the centroid estimate continue be to accurate up to 20th magnitude objects.

5. VALIDATION

The photometric estimates for the simulated cases of PSFs were achieved with around 99 percent accuracy. Until now the images contained only one point source. However, celestial images from telescopes are generally crowded with many sources of brightness around any particular region including but not limited to stars, man-made satellites, galaxies etc. Also, the tails of these sources merge together to produce regions of higher intensity than that of individual sources. The algorithm must be comparably effective in such real cases. In order to compute the effectiveness of the method, an artificial crowded-star-field is constructed and then the photometric estimation is done on it. Chapter 6 describes the image handling procedures such as de-blending of sources, sharpness and roundness criteria, optimal frame size etc. needed during photometric estimation of crowded sources.

5.1 Simulated Crowded Star-field

A crowded star-field with 5 sources in a 50×50 frame is constructed. The parameters used for the sources are given in table 5.1.

Table 5.1. Details of the sources for crowded star-field construction

Source	Z_o**(ADU)**	u_x **(px)**	u_y **(px)**	σ **(px)**
A	3000	27.2	13.1	2
B	600	24	20	1.5
C	300	16.5	24.3	2
D	1500	19	19	1
E	120	25.5	28	2

A randomly varying Sky background with $\lambda = 100$ ADU and a readout uncertainty of 10 ADU are added to the image. Fig. 5.1 shows the constructed image

of a crowded source-field and its intensity model simulating the raw image from a portion of the detector. Images of such types require proper de-blending in order

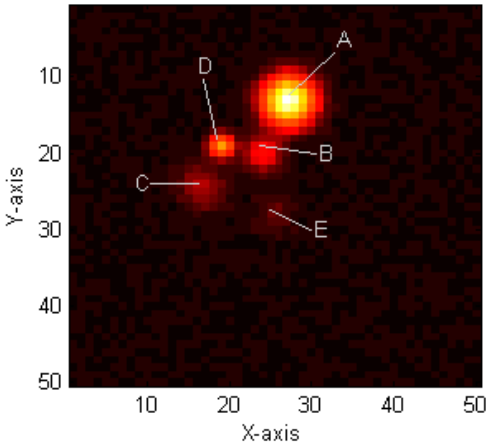

(a) Constructed raw image

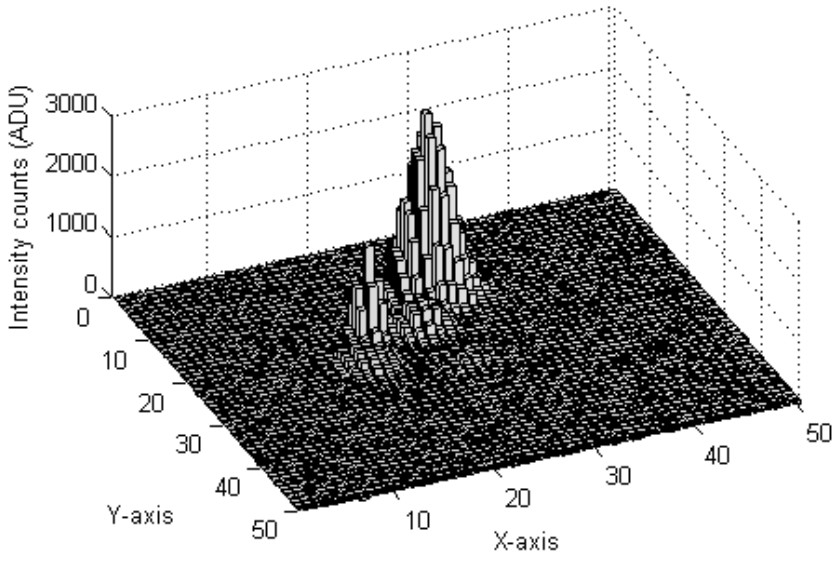

(b) 3d model

Figure 5.1. Constructed image with 5 point sources using given parameters resembles a crowded star-field

to extract information about individual sources fitting to certain criteria. It is observed from repeated simulations that stars with high brightness are easily detected

by the algorithm whereas those having brightness value close to the sky background missed a certain number of detections. Detection also depends on the settings in the de-blending algorithm. A total of 5000 simulations were run and estimates recorded. Table 5.2 lists the mean estimate for the parameters along with the number of missed detections for each source type. The object with the peak value of 120 ADU had the worst detection in the sample.

Table 5.2. Parameter estimated for the sources from the constructed star-field

Source	$\hat{Z}$	$\hat{u}_x$	$\hat{u}_y$	$\hat{Z}$ **error (%)**	$\hat{u}$ **error (px)**	**Missed (%)**
A	2995.7	27.197	13.105	0.14	0.006	0
B	598.7	24.027	19.958	0.22	0.05	0.04
C	299.5	16.505	24.293	0.17	0.009	12.8
D	1484.7	19.01	19.017	1.02	0.02	0.66
E	121.7	25.49	27.99	1.42	0.01	34

5.2 Results

5.2.1 Estimate Precision

Fig. 5.2a shows the scatter plot of the absolute errors in the centroid estimate obtained from sample runs for each of the sources. For A and D (sources with high magnitude), errors are limited to about 0.05. For B and C, the errors are scattered mostly over the range of 0-0.2 pixels. E, the source with lowest magnitude has errors scattered over a wide range of 0-0.5 pixels. Hence A and D have the highest estimate precision while E has the least.

Fig. 5.2b on the other hand shows a similar plot for the percentage error in the peak. The estimate error for A is less than 2%. It varies from 0-5% for D, 0-7% for B, up to 10% for C while it is more than 15% for E. Hence, except for E, the source with lowest magnitude, peaks of other objects can be well estimated with accuracy over 90%.

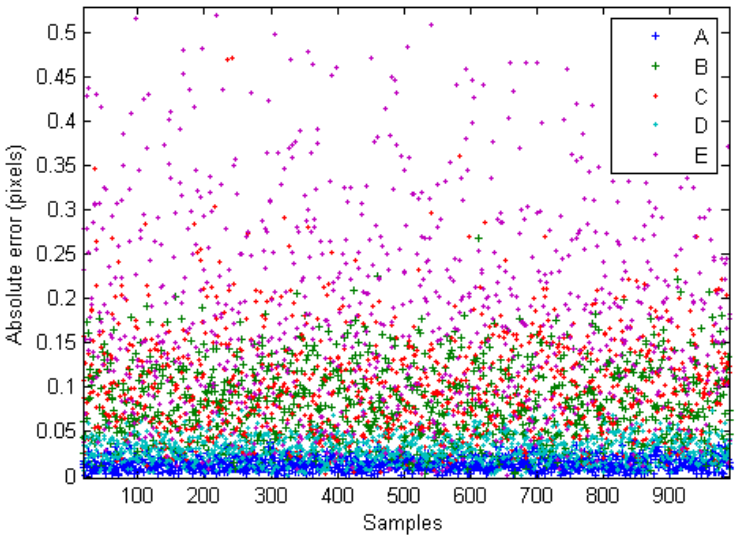

(a) Centroid estimate error

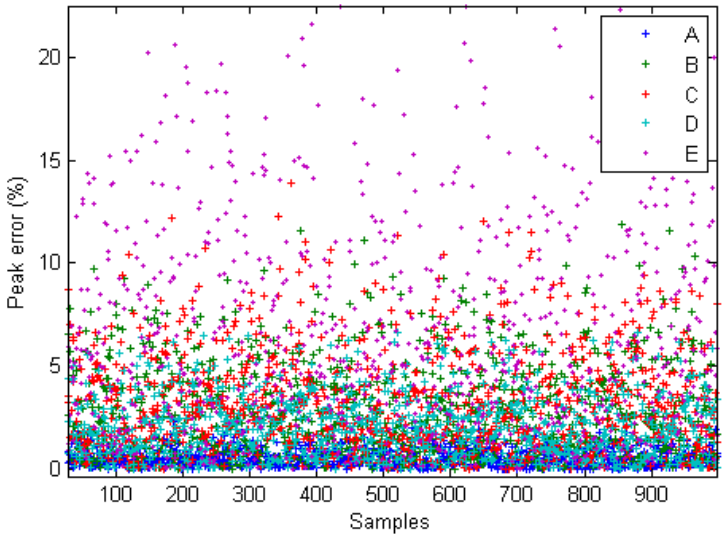

(b) Peak estimate error

Figure 5.2. Absolute error in the centroid and peak estimates for each of the stars in the crowded field

Depending on the precision of the estimate for each of the objects, the performance of the algorithm in actual images of crowded star-fields can be predicted.

5.2.2 Source Detection

The missed detection counts as in table 5.1 are higher in the sources having intensities very close to the sky background. The de-blending algorithm requires linear divisions of the intensities from the background level to the highest in the frame; certain sources with the peak near one of the divisions could get filtered out in the process (however, some parameters in the algorithm govern the trade-off between the computation cost and the detection). In some cases, the signal-to-noise ratios (SNRs) of faint sources can reach quite low in contrast to the brighter sources; it is known that a very faint source does not have the Airy shape and hence cannot be approximated by the Gaussian function [14] (though this was not applicable to the test case). Section 6.5 has further details on de-blending.

5.3 Result from Numerical Optimization

For a comparative analysis of the method developed in this work with a popular numerical method, the Maximum-likelihood estimator (as explained in section 2.3) is used together with the Newton optimization routine in order to obtain the parameters of the approximated Gaussian PSF. However for simplicity, and because the numerical method had convergence issues, the standard deviations σ_x and σ_y were set as uncorrelated (i.e. $\rho = 0$). Results from both the methods are compared.

Fig. 5.3 shows the rms error in the centroid estimates for the sources using both the methods. X-axis is for the objects in the decreasing order of their relative brightness. The estimates from the LS 2D analytical method are found to be slightly better than those from the numerical method. This could be explained by the use of the analytical expression to obtain explicit values for the centroids (equation [3.30]). (The numerical method on the other hand, need to find the local maxima).

Note that similar to the LS 2D estimator, the maximum likelihood estimator used in this comparison was not efficient; since the measurement model was biased (based on the first order approximation).

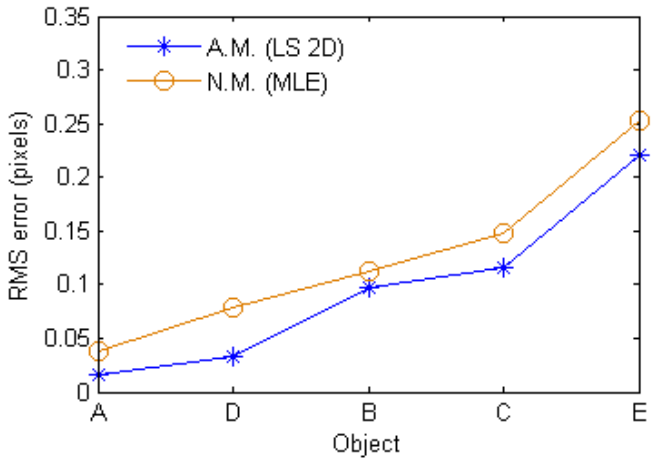

Figure 5.3. RMS error in the centroid estimates from the LS 2D and the ML estimators. Objects are in the decreasing order of their relative brightness.

6. IMAGE HANDLING PROCEDURE

Before implementing the estimation algorithm on a raw image, certain procedures need to be followed for efficient image data utilization.

6.1 Sensor Pixel Data

Photons enter the camera aperture and strike the detector array transferring energy in form of free electrons. Depending on the quantum efficiency of the detector, most of these electrons are collected by the preprocessor. After the integration and processing (analog to digital conversion), data is delivered at the output in a raw form (called as raw image). These raw images are made up of numeric values of intensities. Since raw images are uncompressed, each numeric value is proportional to the photon count of the sensor pixel. Hence, these numeric values are used for image processing.

Square Measurement Frame

Generally, an image of the point source occupy more than one pixel. In some cases, the blur is spread across multiple pixels on all sides of the centroid.

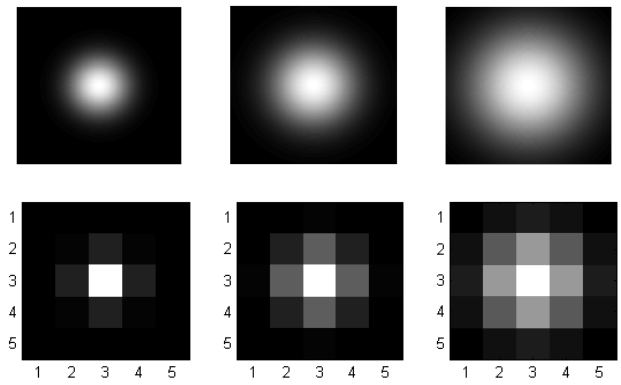

Figure 6.1. Pixelated image of the Gaussian PSF. Round PSF is translated into square pixels.

Fig. 6.1 shows three different Gaussian PSFs with the corresponding pixelated data when using 5×5 measurement window. It can be noted that although the shapes of the PSFs are circular, the image data in the sensor array is defined by choosing a square window and not the circular. Since, most of the PSFs have only a few pixels of the radius, using a square frame is well suited and sufficient for the case. In addition, using square/rectangular frame is convenient for coordinate calculations. Hence, rectangular measurement window was used in this work.

6.2 Background "Sky" Calculation

It is understood that the data output from each individual pixel of the sensor array is composed of the source signal and other background noises. While source signal depends on the power of the object of interest (such as a star), background noises depend on the power of the contaminating sources such as diffused lights from sky and lights from other celestial bodies. In addition to the background noise, sensor adds its own readout noise to the data. This readout noise is constant and it depends on the quality of the sensor.

In order to model the profile of the object of interest, the background should be estimated for an appropriate deduction from the measurement. The background level so obtained is deducted from the pixel data on pixel basis. It is important to accurately determine the background variations for both distinct as well as highly blurred and faint sources, especially for the blurred sources where object brightness is extended to a larger area and hence there is a combined influence of the point source and other noises on background estimation.

A number of methods have been developed to estimate the background sky level from the pixel data.

6.2.1 Using $k.\sigma$ clipping

One of method utilizes estimation by $k.\sigma$ clipping around the center of the local frame data [34]. The center is usually chosen as the median for robustness; sigma σ, the deviation around the center as standard deviation. In this method, basically those frames data is clipped which satisfy the following relation. This process is iterated until convergence.

$$m - k.\sigma < c < m + k.\sigma \tag{6.1}$$

where m = center of the local frame data, median

k = factor for sigma, by default 3

σ = deviation around the center, by default standard deviation

c = clipped background

6.2.2 Using Mode Estimation

Another method utilizes mode estimation as a robust estimate of the background [34]. However, it requires an optimal bin width of the histogram for the observed data. There are many methods to find the optimal bin width (see the subsection).

Once the optimal bin width is found, a histogram is generated to determine which interval contained maximum number of entries of the pixel intensity counts. Having known that interval, mode is then calculated by taking the mean of all the entries falling in that interval.

Bin width obtained using Freedman-Diaconis rule [35]

The Freedman-Diaconis rule has been used by Astronomers and Astrophysicists in developing star cataloging programs (e.g. Astropy Package [36]). The method utilizes rank-based statistics for results and has advantage of being more robust to deviations from a normal distribution. It is based on the equation 6.2

$$\Delta_b = \frac{2(q_{75} - q_{25})}{n^{\frac{1}{3}}} \tag{6.2}$$

where $q_N = N$ percentile of the data, n = Number of data points (or pixels)

Bin width based on the average interval between min-max peak counts over the entire frame pixels

In this method, at first the minimum and maximum peak counts (in ADU) are extracted from the observed data array. Next, it is divided into equal intervals given by equation 6.3. The number of intervals should be equal to the number of pixels in the candidate local frame.

$$\Delta_b = \frac{I_{max} - I_{min}}{n} \tag{6.3}$$

where

I_{max}, I_{min} = magnitude of maximum and minimum peak counts respectively

n = Number of data points (or pixels)

Although this method worked very efficiently during simulation runs, some author regard this as fundamentally wrong [34].

Depending on how crowded the stars are in the observed image, sometimes a combination of $k.\sigma$ and mode estimation is used to obtain the background level [37].

Fig. 6.2 shows the plots of the absolute error in the estimated peak for various frame sizes when simulated using the three background calculation rules. For this comparative analysis, Gaussian PSFs were generated with the following parameters.

Amplitude, $A = 1000$ ADU

Frame size $= \{3, 5, 7, 9, 11, 13, 15, 20\}$

SNR $= \{2, 3, 5, 10, 20, 100\}$

$\Sigma_1 = \begin{pmatrix} 1 & -0.75 \\ -0.75 & 1 \end{pmatrix}, \Sigma_2 = \begin{pmatrix} 2.25 & -0.75 \\ -0.75 & 2.25 \end{pmatrix}, \Sigma_3 = \begin{pmatrix} 4 & -0.75 \\ -0.75 & 4 \end{pmatrix}$

Added to the image was a sky background with Poisson parameter, $\lambda = 100$.
Hence, the final raw data was the resultant of Gaussian and Poisson statistics.

From the figures, one can infer that Mode estimator based on min-max averaging on the pixel counts provided better result than the other two. Several simulations

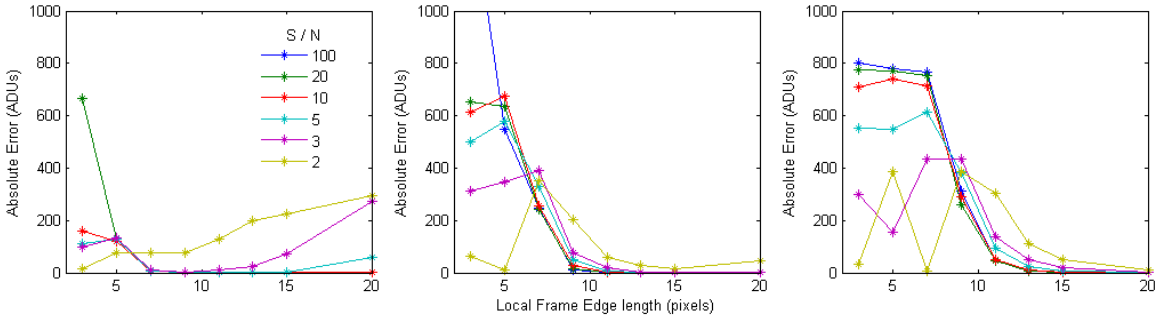

(a) 3σ mean clipping

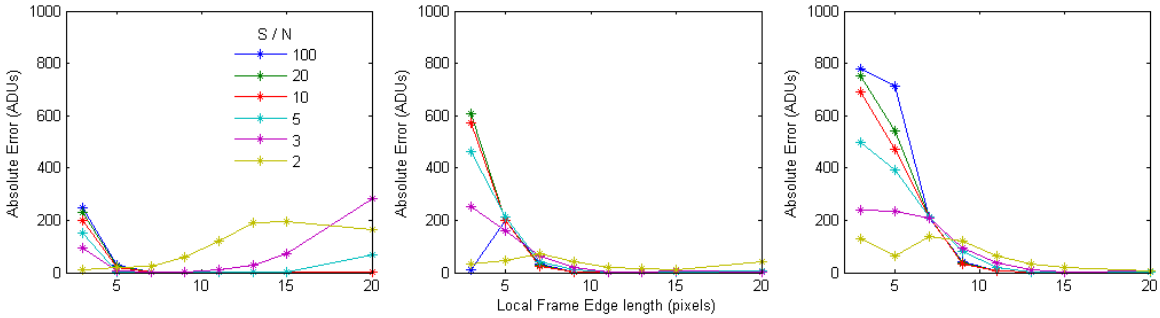

(b) Mode estimation by Freedman-Diaconis rule

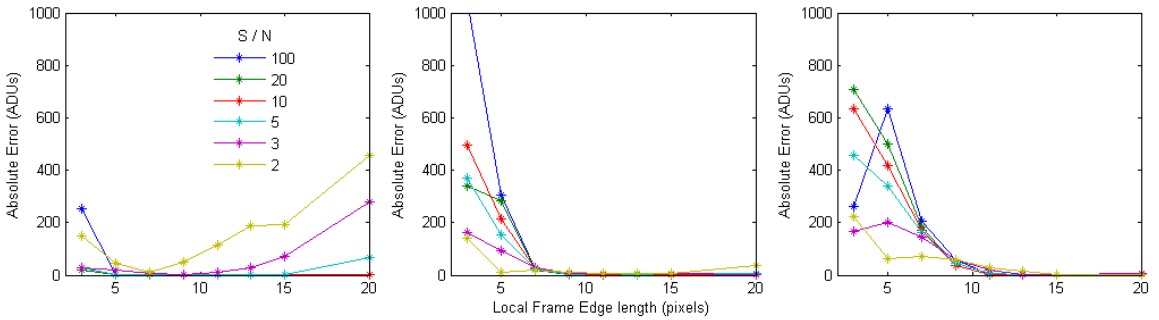

(c) Mode estimation, min-max averaged

Figure 6.2. Absolute error in the peak estimate of Gaussian PSF with given SNR and increasing covariances: Σ_1, Σ_2 and Σ_3 from left to right respectively. Background deductions are based on the three methods described. Notice all the leftmost graphs; since the PSFs have smaller width, the errors are higher for larger frames as well (apart from smaller frames) beacuse of the over sampling of the background. In between the two, there is a region of optimum frame sizes producing smaller errors.

Table 6.1. Accuracy of the estimate for different background subtraction rules

	$\sum_1$			$\sum_2$			$\sum_3$		
Background Estimation Rule	**Frame size and accuracy of the estimate**								
	3×3 5×5	7×7 9×9	13×13 15×15 20×20	3×3 5×5	7×7 9×9	13×13 15×15 20×20	3×3 5×5	7×7 9×9	13×13 15×15 20×20
3σ mean clipping	Poor	Good	Good	Poor	Avg.	Good	Poor	Poor	Poor
Mode estimation - using *Freedman-Diaconis* rule	Avg.	Good	V. Good	Poor	V. Good	V. Good	Poor	Avg.	Good
Mode estimation - using *min-max averaged* bin width formula	Good	V. Good	V. Good	Avg.	V. Good	V. Good	Poor	Good	Good

were run to test the hypothesis. Table 6.1 shows the result of those simulations based on all three types of background deduction rule. It compares the accuracy of estimated peak from the sample data in small to large windows size and with various width (achieved by varying covariances, Σ) of point sources.

6.3 Optimal Local Frame Size

One can notice the poor accuracy and higher error occurrences in smaller $\{(3 \times 3), (5 \times 5)\}$ and some medium $\{(7 \times 7), (9 \times 9)\}$ sized frames. From several simulations, it is observed that the profile generation requires pixel counts per frame to be high enough; and that the frame size be larger compared to the set radius of the PSF- mostly to have adequate number of samples from the blur for the fitting algorithm to work. When the entire frame is occupied by the high brightness of a point source without much of its tail information, the estimator is unable to fit in a correct Gaussian to the profile. Hence the algorithm fails to give accurate result for smaller frames.

Moreover, when point sources have smaller spread, the errors are limited to the smaller frames but when sources have larger spread, the errors propagate toward larger frames as well (see fig. 6.2).

Generally, it is difficult to preset sizes of frames for point-sources of different brightness and unknown spread. At the same time, if we are to find the background deduction simultaneously while finding the centroid and peak, we need to consider a suitable size of the mesh that has just enough data for the source and the sky noise. Following calculation obtains optimal frame size based on empirical data from several simulations using min-max averaged mode estimation rule for background deduction. Only those estimates which were above 95% of actual were considered accurate for this purpose.

$$\text{Sample size} = 50000$$

$$\text{SNR} = 2, 3, 5, 10, 20, 100$$

$$\text{Frame edge length (pixels)} = 20, 15, 13, 11, 9, 7, 5, 3$$

Case Σ_1: Given $\sigma_1 = 1$, optimal frame edge length = {5, 7, 9}

Case Σ_2: Given $\sigma_2 = 1.5$, optimal frame edge length = {7, 9, 11, 13, 15}

Case Σ_3: Given $\sigma_3 = 2$, optimal frame edge length = {11, 13, 15, 20}

It is observed that minimum size of frames in each of the cases had a similarity. This was true for maximum sizes as well. In all of the cases, the minimum and maximum size of the frame depended on the standard deviation, σ of the profile. The ratio of minimum or maximum frame size with the standard deviation was approximately constant, equal to a multiple of FWHM[1] of the profile.

[1]FWHM: Full Width at Half Maximum refers to the width of the Gaussian profile (or other curve with no sharp edges) where the peak value is exactly halved or the curve is at half maximum value. FWHM is generally used to compare quality of Point sources which do not have a fixed width as in case of Gaussian profiles.

Mathematically, that constant was found to be close to twice the FWHM of the PSF for minimum edge length and four times FWHM for maximum edge length.

$$\frac{\text{frame edge length, } n \text{ pixels}}{\text{Standard deviation, } \sigma \text{ pixels}} \approx constant \tag{6.4}$$

Minimum frame size:

$$\text{Case} : \sigma_1 = 1 : \quad 2(FWHM_{\sigma_1}) = 2 \times 2.3548 \times 1 = 4.71 \approx 5$$

$$\text{Case} : \sigma_2 = 1.5 : \quad 2(FWHM_{\sigma_2}) = 2 \times 2.3548 \times 1.5 = 7.1 \approx 7$$

$$\text{Case} : \sigma_3 = 2 : \quad 2(FWHM_{\sigma_3}) = 2 \times 2.3548 \times 2 = 9.4 \approx 9$$

Maximum frame size:

$$\text{Case} : \sigma_1 = 1 : \quad 4(FWHM_{\sigma_1}) = 4 \times 2.3548 \times 1 = 9.4 \approx 9$$

$$\text{Case} : \sigma_2 = 1.5 : \quad 4(FWHM_{\sigma_2}) = 4 \times 2.3548 \times 1.5 = 14.1 \approx 15(\text{nearest})$$

$$\text{Case} : \sigma_3 = 2 : \quad 4(FWHM_{\sigma_3}) = 4 \times 2.3548 \times 2 = 18.83 \approx 20(\text{nearest})$$

Above result can be observed in the error plots 6.2c. This empirically obtained result for minimum edge length is co-incidentally same as the critical sampling size of 2 pixel/FWHM for faint sources [13]. Fig. 6.3 shows the Gaussian profile for a point source with peak magnitude = 1000 ADU and σ = 1 pixel. A length of 5 pixels is the minimum required to cover 2(FWHM) of the profile.

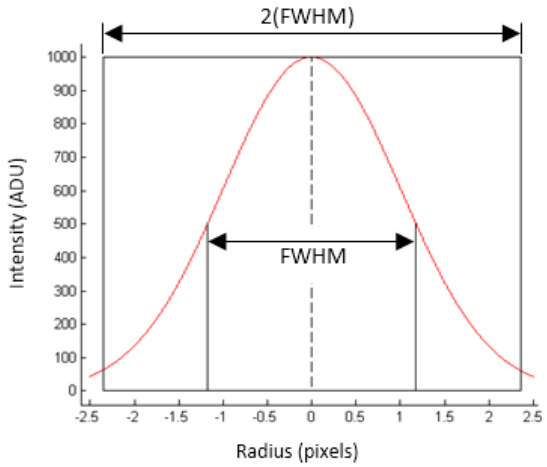

Figure 6.3. For a point source, the minimum and maximum sizes of the local frame is proportional to the FWHM of the PSF

6.4 Precaution During Background Correction

Inclusion of surrounding pixels is essential for correct background determination. On the other hand, one must take care while including the number of background dominated pixels in the frame. If the background dominated pixels are larger in number compared to the bright pixels from the point source, the estimate for the background becomes prominent. Thus, subtraction is not done properly and the apparent brightness flux of point source decreases [38]. This phenomena also occurs in case of faint objects where background dominates the point source. Therefore an optimal size of the local frame must be found.

Sometimes, it is difficult to obtain an adequate number of data points to locally determine the sky background. For example, in case of the crowded star-fields, sources are located very close to each other causing the background calculation routine to mistakenly compute a high background to be subtracted. This in turn leads to the loss of useful PSF data from the sample, resulting in a poor estimate. To work around such situation of less than critical number of data points, it has been suggested that the value of background be obtained from a larger region of the image (like 25×25) and not the local frame [13, 34]. However, including a very large region of the image (for example 1000×1000) could result in poor background estimation especially in case of non-flat sky noises. Besides, the frame size is found to affect the performance of the de-blending algorithm in this work (discussion in section 6.5).

Fig. 6.4a plots percentage error in the peak estimates obtained after local and regional background subtractions. Similarly, 6.4b plots RMS errors in the centroid estimates. It can be observed from the plots that calculating local backgrounds against regional drastically decreased the accuracy of the estimates. Furthermore, it is found from the simulations that there is a sudden increase in the number of failed detections. The algorithm in this work obtains the background from windows of reasonable sizes (25×25, 50×50 etc.) and not local or the entire image at once. Note that only background levels are calculated from these windows. Gaussian fitting

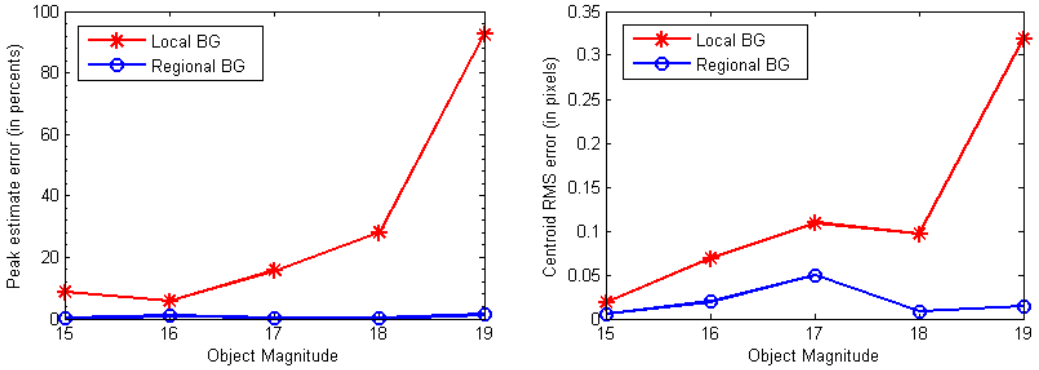

(a) Peak error (b) Centroid error

Figure 6.4. Effect of subtracting local background as against regional background

for the PSF is obtained from an optimal size frame around the PSF as discussed in the previous section.

6.5 De-Blending Crowded Field Sources

Sometimes the observation frame is crowded with multiple sources positioned next to one another in the image (for example fig. 5.1a). Therefore, the pixel counts between two close sources are affected by both. The de-blending procedure by Beard and MacGillivray [39] comes useful in identifying and locating sources in such complicated arrangements. Fig. 6.5 shows the 2d model for the intensities of a crowded field.

The following steps are followed in the de-blending method.

1. At first, the global background level is determined and subtracted from the frame. (Zone 1 with the black pointer in the 2d model represents the global background level).

2. Once the background is subtracted from the entire frame, the remaining intensity counts are divided into equal sections (generally 16 sections) starting from the new minimum to the new maximum in the observation window.

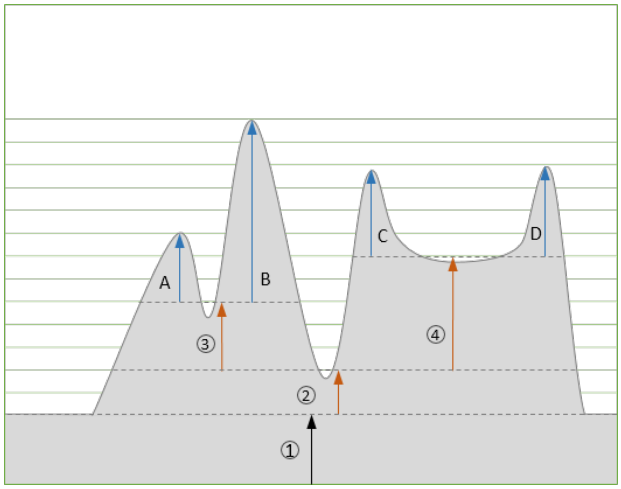

Figure 6.5. De-blending procedure for a crowded source

3. The de-blending routine now recursively moves through each section starting from the bottom looking for separate objects.

4. As soon as the number of objects is found to increase at a particular section (at the upper end of zone 2 in the figure), that section is recorded as the local background for the next search of objects. The routine now processes separate objects individually (zone 3 and 4)

5. If at some point while going through the sections in any of the objects no new separations are found, the object is noted as one single point source (A, B, C, D). The parameters are then determined using observation data above the local background level (3 and 4 in the figure). This local background (plus other local backgrounds, if any) is later added to the estimates in order to obtain results at the global background level.

6. Although the procedure is able to determine individual objects in a crowded field, those objects are still approximations of actual sources since it is unlikely to completely resolve nearly merged objects.

6.6 Sharpness Criteria - False Detection Due to Sensor Flaws and Cosmic ray events

Sometimes, cosmic ray events or some sensor flaws can create bright spots of a few pixels on the frame. Unlike real object images, these cosmics are characterized by the sharp edge in the brightness from one pixel to another. These spots when detected by the algorithm can lead to false detections. In order to filter out such outliers, several empirical methods have been developed. [3, 34]. According to one of the methods, these spots can be identified by finding the ratio of the intensity difference between observed maximum and the mean of its surrounding pixels to the best estimate of the spot.

$$\text{Sharpness} = \frac{\Delta D_{obs}}{H_{est}} \tag{6.5}$$

where $\Delta D_{obs} = D^*_{i,j} - D_{i,j}$

$D^*_{i,j}$ = Observed maximum intensity

$D_{i,j}$ = mean of pixels surrounding $D^*_{i,j}$

H_{est} = best estimate from the algorithm

When a non-celestial object such as a narrow spot is encountered, which has most of the brightness centered at one pixel while surrounding pixels have low intensities, the algorithm fits a profile with low intensity at its center. This gives the value of (Sharpness ≥ 1). On the other hand if a low lying spot is found, the value of sharpness is very close to 0. By setting an appropriate limits, these false detections could be minimized since most of the celestial objects would have moderate sharpness. Fig. 6.6 illustrates the output of the algorithm showing good as well as bad detections from an image.

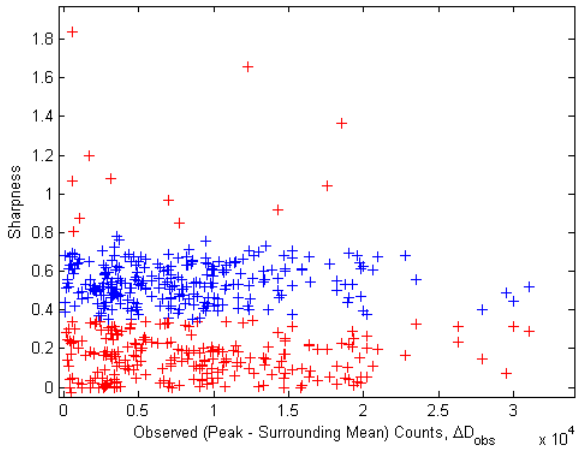

Figure 6.6. False detection shown by red '+' while good ones by blue '+' obtained using Sharpness Criterion. All the false detections in this particular simulation were those whose sharpness criterion were outside ($0.35 < \text{Sharpness} < 0.8$)

6.7 Shape Criteria - To Filter Light Streaks of Moving Objects

A very fast moving object which is not very well captured in the frame should not be extracted from the image and used in centroiding. The same applies when a very bright object is imaged by the camera. Too many photoelectrons may collect within the pixel of the CCD causing the charge to overflow to the neighboring pixels. This happens when more photoelectrons are received than the full well capacity of the CCD.[2] The charge overflow from the pixels causes what is known as "bleeding". It is visible as a narrow streak of light across many pixels in the raw image. These light streaks could be detected by the algorithm as a highly elongated source leading to false detection.

Similar to the sharpness criteria for eliminating false detections, the shape criteria helps in filtering out the undesired light patterns - patterns which are highly elliptical in shape. It works by approximating the observed counts by two one-dimensional Gaussian function (similar to 2d approximation), orthogonal to each other [34]. The

[2] "The amount of charge a pixel can hold in routine operation is termed its full well capacity" - Howell [5]

respective widths or spreads σ_x and σ_y thus estimated are used to determine the value of the shape criterion from equation 6.6. Note that, since the parameter estimator developed in this work obtains σ_x and σ_y together, constructing two one-dimensional Gaussian is not required.

$$\text{Shape} = \frac{\sigma_x^2 + \sigma_y^2}{\sqrt{\sigma_x^2 + \sigma_y^2}} \tag{6.6}$$

Depending on the value of this criterion, certain objects can be filtered out by the algorithm. From the simulations, it is found that a value of (Shape < 5) provides a good filtering of highly elliptical undesired light patterns from the image.

Fig. 6.7a shows objects tagged in a crowded field by the existing algorithm; even

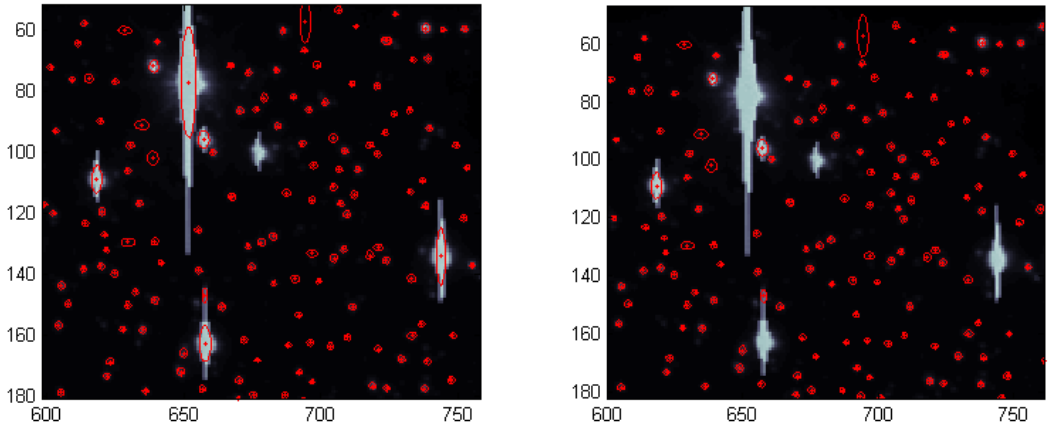

(a) Existing algorithm

(b) With shape criteria

Figure 6.7. Shape criteria to filter objects with undesired light patterns

the sources which did not have well defined round shape (objects with longer streaks of light) have been detected along with others objects. This will definitely lead to a wrong identification of the actual source. The next image 6.7b is generated by applying the shape criterion: only those objects which passed the criterion are identified to be tagged.

Summary

Fig. 6.8 shows an overview of the PSF parameters estimation. The sharpness and shape criteria are optional and could be excluded from the main algorithm, if needed.

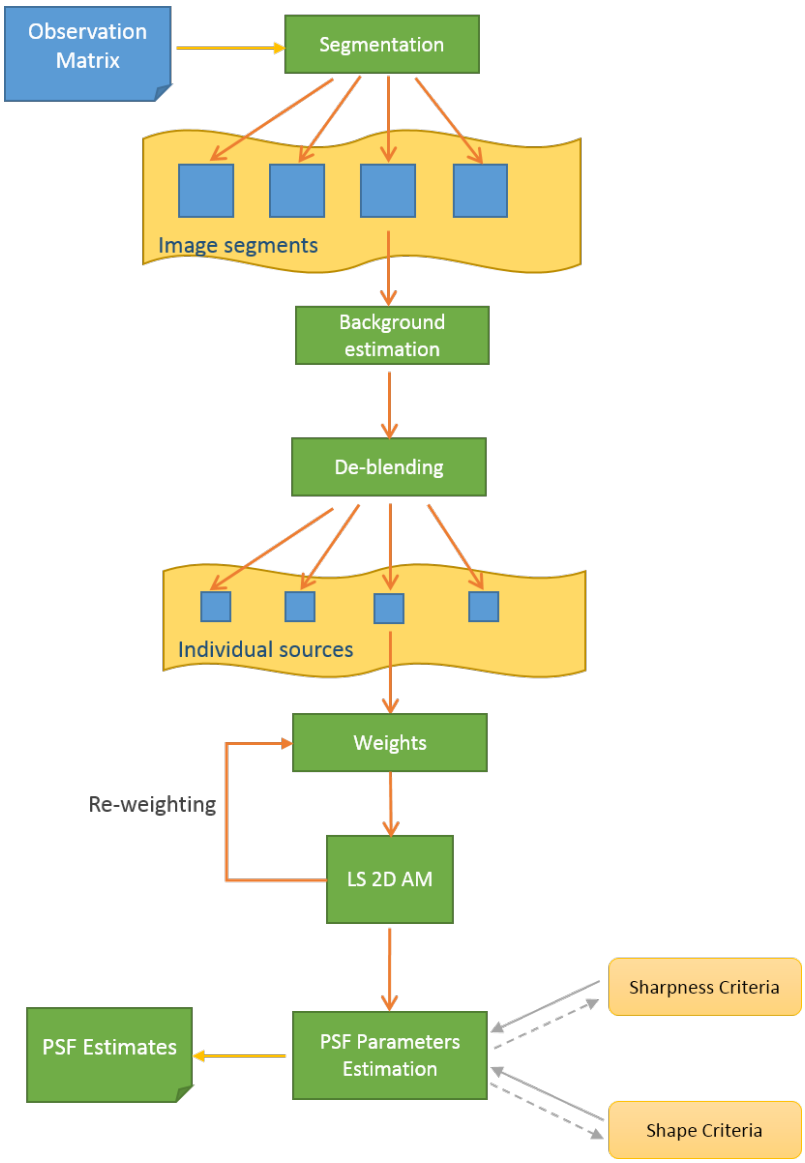

Figure 6.8. Flowchart of the PSF approximation process

7. APPLICABILITY OF THE ALGORITHM

7.1 Simulation on a Real Celestial Image

Since the algorithm is developed for the intended purpose of celestial photometry, it is essential to simulate celestial images and determine the applicability of the method. A test image shown in fig. 7.1 is obtained from the Smithsonian Astrophysical Observatory telescope datacenter [40]. The image contains celestial objects with brightness ranging from -14 to -5 magnitudes (instrumental).

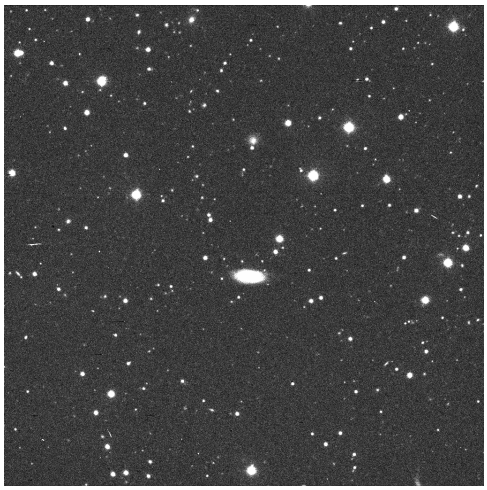

Figure 7.1. A test image from Smithsonian Astrophysical Observatory telescope datacenter [40]

The image has the following informations

α, RA: 16:151:30.993 - 16:16:22.690 J2000

δ, Dec: +31:19:36.30 - +31:30:36.92 J2000

Dimensions = 1024 $\times$ 1024

Resolution = 0.644574 arcsec/pixel

At first the FITS WCS of the image was fixed using WCStools [41]. In this process, the header of the FITS file was updated with correct coordinate information. Then

the information about the stars in the image was retrieved from the catalog USNO-B1.0 [42]. In the next step the X and Y coordinate of the objects are determined from their respective right ascension and declination information. The centroids obtained from the LS 2D analytical method is then compared with these coordinates from the catalog and results noted.

Fig. 7.2 shows the plots of the centroids obtained from the the LS 2D AM as well as the catalog. Magenta colored diamonds are the catalog stars while the green boxes are the sources detected by the analytical method. Note that the catalog shows top 300 brightest stars present within the region and are found from many observations over period of time. On the other hand, the LS 2D method detected sources using only this image.

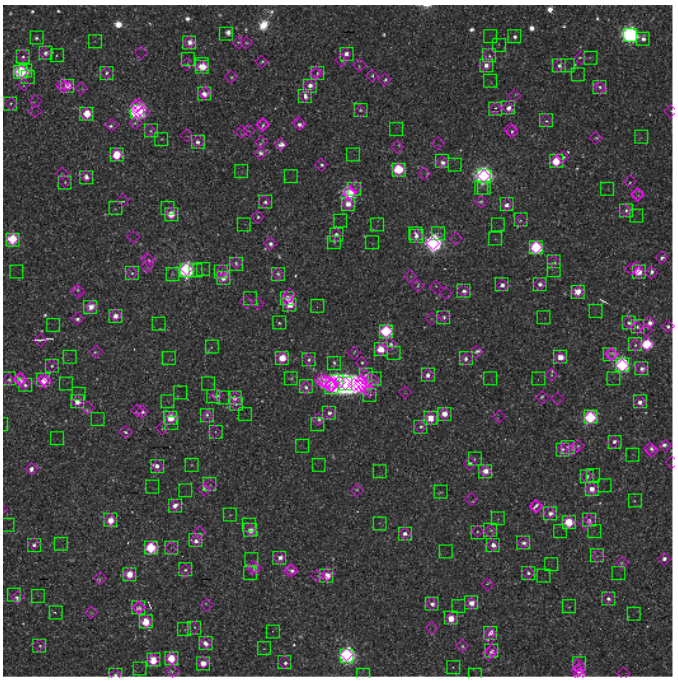

Figure 7.2. Plots of centroids from analytical method and the catalog in green and magenta boxes respectively

The centroid determined from LS 2D analytical method is compared with the catalog data in a graph. Plot 7.3 shows the relative error of the centroid from LS 2D

analytical method with respect to the catalog. The catalog data is considered as the base line. The graph is for only those stars which were found to be within unit pixel radius of the cataloged position.

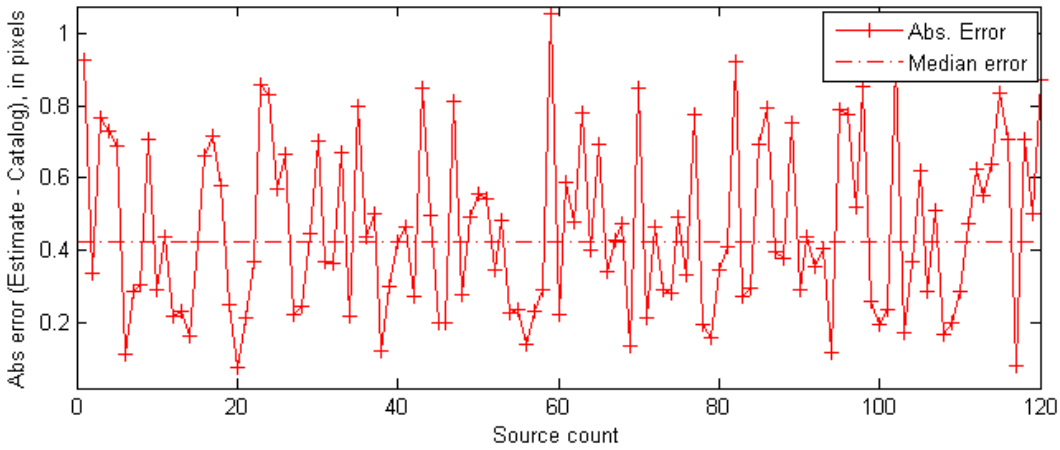

Figure 7.3. Absolute error in the LS 2D centroid estimates with respect to cataloged centroid

7.2 Results from an Astronomical Software

To have a direct comparison with one scientific tool used to identify and catalog objects in images, a popular astrometry software, S-Extractor [37] developed by Emmanuel Bertin is used. S-Extractor determines centroid using isophotal data from the observation which is similar to using the center of gravity method. (Another approach is based on windowed centroid estimation). The software is widely used in the analysis of astronomical images. Faster execution and the ability to accept user supplied inputs for various parameters are the main features of the software.

S-Extractor is used to detect sources and locate their centroids in the same image. The results are plotted on a graph along with those of LS 2D and the US No-B1 catalog data. Image 7.4 shows the plots of stars isolated from all the detections - stars

which were estimated by LS 2D and S-Extractor to be within unit pixel radius from the cataloged centroid.

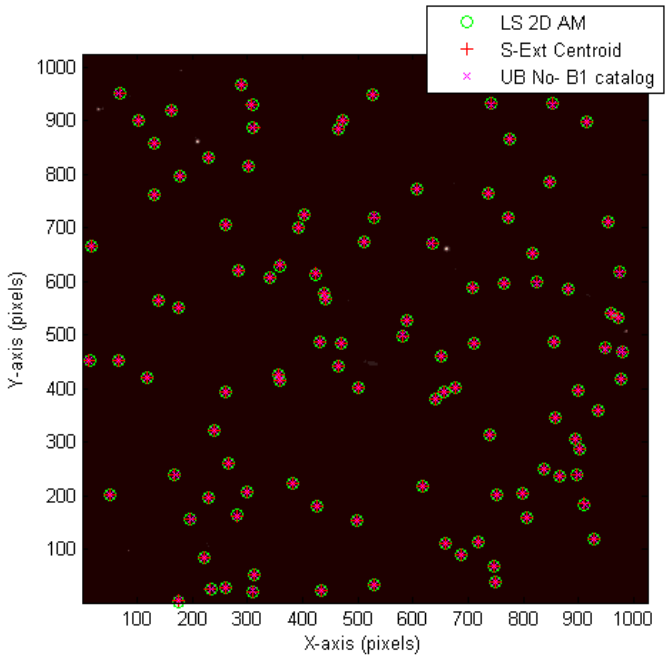

Figure 7.4. Plots of identical centroid estimates from LS 2D, S-Extractor and the US No-B1 catalog isolated from all the detections

Similar to the earlier absolute error plot, fig. 7.5 shows the absolute error in the centroid estimate from the two methods with respect to the cataloged stars. Again, only those stars are considered which were up to unit pixel radius away from the cataloged position.

It could be observed from fig. 7.5 that the LS 2D centroid errors are almost close to that of the S-Extractor's. In few of the stars, the analytical method actually outperformed the other. The standard deviation of the LS 2D error is found to be better than that of S-Extractor, thereby showing higher precision for this image. The mean error for S-Extractor was slightly lower on the other hand. This could probably be attributed to the additional filtering and correction subroutines employed within the S-Extractor application. Nonetheless, the analytical work is shown to

have obtained centroid with high accuracy. Additional figures could be found in the appendix.

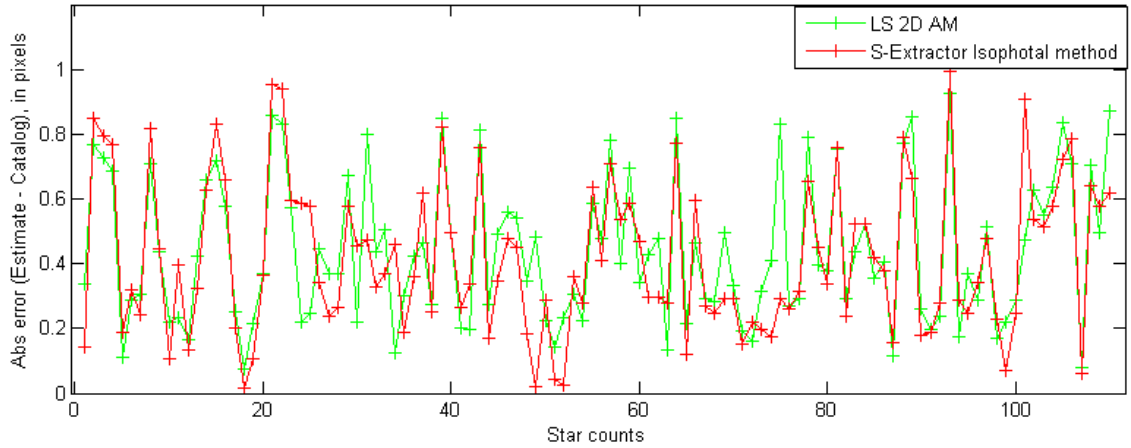

Figure 7.5. Absolute error in the centroid estimates from the two methods with respect to cataloged centroid

8. CONCLUSION

The tracking and cataloging of near Earth space objects relies mostly on ground based observations. Due to the great distance of the objects from the observation site only non-resolved object images are obtained. The CCD used in optical systems generate raw celestial images from which individual object's astrometric position are extracted. In order to do so, the center of the object's image on the CCD frame has to be found. However, the observation frames that are read out of the detector are subject to noises from three different sources: celestial background sources, the object signal itself and the sensor.

An analytic method based on least squares 2-dimensional approximation is developed keeping in mind the noises present in the total signal. Since the detector array outputs discrete pixels counts, the observations are Poisson distributed. However, the readout introduces Gaussian distributed error. Hence, the overall observation is based on combined Poisson-Gaussian statistics. The blur formed by light sources known as point spread function have the Airy disc (and pattern) which in turn can be approximated to the Gaussian intensity function. As long as the observation data has sufficient and suitable photon counts, the point spread function can be modeled with a Gaussian profile. The analytic method obtained a solution for the least squares minimization of the error between the observation and a model Gaussian point spread function. It is observed that the presence of noise in the measurement reduced the estimate accuracy because of improper sampling of the tail data. Therefore, to improve the influence of low count - low SNR tail data, weights determined by expanding the least squares error function are incorporated. Additionally, since the measurements are normally biased due to the elimination of higher order terms in the measurement model, the solutions are found by iterating the fitting procedure while updating the weights and therefore minimizing the bias. An optimal number of iterations has been

empirically determined for various signal to noise ratios. At the end of those iterations, the Gaussian parameters are found by solving simple equations.

The least squares 2d analytic method is applied for identifying sources in simulated crowded and non-crowded fields. The estimates for centroids and peaks are validated. In any crowded source image, the number of good detections depend on the user supplied inputs for various subroutines within the image handling procedure. The analytic method is eventually tested on a real celestial image to estimate the centroid information. At the same time it showed comparable estimate accuracy with respect to the astronomical tool even though the former didn't use additional filtering and corrections unlike the other. These results demonstrate the applicability of the algorithm for astronomical image analysis. In a separate observation, it is found that the least squares 2d analytic method outperformed a numerical method for the test case. Certain assumptions were made in this work to simplify the estimation. An in-depth analysis on those will further enhance the accuracy of the estimates.

LIST OF REFERENCES

LIST OF REFERENCES

[1] J. C. Liou. A parametric study on using active debris removal for LEO environment remediation. In *Proceedings of the International Astronautical Congress*, volume A6.2.5, Prague, Czech Republic, Sept 2010.

[2] United States strategic command (USSTRATCOM) Joint space operation center(JSpOC). https://www.stratcom.mil/factsheets/11/Space_Control_and_Space_Surveillance/.

[3] C. Frueh. *Identification of space debris*. Shaker Verlag, 2011.

[4] James Dick Timothy D. Maclay Firooz A. Allahdadi Jonathan Marchant, Simon Green. Real-time ground-based optical detection system for space debris. In *Characteristics and Consequences of Orbital Debris and Natural Space Impactors*, volume 2813(1), pages 22–31, August 1996.

[5] S. B. Howell. *Handbook of CCD astronomy*. Cambridge university press, 2nd edition, 2006.

[6] By Sloan Digital Sky Survey(SDSS). http://www.sdss.org/dr6/instruments/imager/index.html.

[7] Photo by Gustaaf Prins on Flickr(CC BY-NC 2.0). https://www.flickr.com/photos/zoeff.

[8] F. Sanson and C. Frueh. Noise quantification in optical observations of resident space objects for probability of detection and likelihood. In *Proc. AIAA/AAS Astrodynamic Specialist Conference*, volume AAS 15-635, Vail, Colorado, August 2015.

[9] Gerald M. Daniels. A night sky model for satellite search systems. *Optical Engineering*, 16(1):66–71, January-February 1977.

[10] Photo by Alan L on Flickr (CC BY 2.0). https://www.flickr.com/photos/35188692@N00/2282306375.

[11] Harrison H. Barrett, Christopher Dainty, and David Lara. Systems likelihood methods in wavefront sensing: stochastic models and likelihood functions. *Journal of Optical Society of America A*, 24(2):391–414, February 2007.

[12] C. Frueh and Moriba K. Jah. Detection probability of Earth orbiting objects using optical sensors. volume 13. American Astronomical Society, 2013.

[13] Michael V. Newberry. Signal-to-noise considerations for sky-subtracted CCD data. *Publications of the Astronomical Society of the Pacific*, 103:122–130, January 1991.

[14] W.J. Merline and Steve B. Howell. A realistic model for point-sources imaged on array detectors: the model and initial results. *Experimental Astronomy*, 6:163–210, 1995.

[15] G. B. Airy. On the diffraction of an object-glass with circular aperture. *Transactions of the Cambridge Philosophical Society*, 5(2):283, Jan 1835.

[16] Jakob J. Stamnes. Focusing of a perfect wave and the Airy pattern formula. *Optics Communications*, 37:311–314, January 1981.

[17] M. Born and E. Wolf. *Principles of Optics*. Pergamon Press, 1965.

[18] W.T. Welford. Aberrations of the symmetrical optical system. *London: Academic Press*, 01/1974, 1974.

[19] R Castaneda and J Kross. PSF measurements using an Airy pattern as test object. *Pure Appl. Opt.*, 3:259–268, 1994.

[20] Alex Small and Shane Stahlheber. Fluorophore localization algorithms for super-resolution microscopy. *Nature Methods*, 11(3):267–280, March 2014.

[21] B. Richards and E. Wolf. Electromagnetic diffraction in optical systems. ii. structure of the image field in an aplanatic system. In *Proceedings of the Royal Society of London*, volume 253 of *Series A, Mathematical and Physical*. Royal Society, December 1959.

[22] Wayne Rasband. ImageJ: Image processing and analysis in Java. http://imagej.nih.gov/ij/index.html.

[23] Bo Zhang, Josiane Zerubia, and Jean-Christophe Olivo-Marin. Gaussian approximations of fluorescence microscope point-spread function models. *Applied Optics*, 46(10):1819–1829, April 2007.

[24] Tjorven Delabie, Joris De Schutter, and Bart Vandenbussche. An accurate and efficient Gaussian fit centroiding algorithm for star trackers. Space Flight Mechanics Meeting, Kauai, Hawaii, February 2013.

[25] R. C. Stone. A comparison of digital centering algorithms. *The Astronomical Journal*, 97(4), 1989.

[26] A. Vyas, M. Roopashre, and B. R. Prasad. Improved iteratively weighted centroiding for accurate spot detection in laser guide star based Shack Hartmann sensor. In *Proceedings of SPIE*, volume 7588, 2010.

[27] K. Levenberg. A method for the solution of certain non-linear problems in least squares. *Quarterly of Applied Mathematics*, 2:164–168, 1944.

[28] Alessandro Foi, Mejdi Trimeche, Vladimir Katkovnik, and Karen Egiazarian. Practical Poissonian-Gaussian noise modeling and fitting for single-image raw-data. *IEEE transactions on image processing*, 17(10), October 2008.

[29] Nathan Hagen and Eustace L. Dereniak. Gaussian profile estimation in two dimensions. *Applied Optics*, 47(36):6842–6851, December 2008.

[30] Kim A. Winick. Cramer-Rao lower bounds on the performance of charge-coupled-device optical position estimators. *Journal of Optical Society of America A*, 3(11):1809–1815, November 1986.

[31] Hongwei Guo. A simple algorithm for fitting a Gaussian function [DSP tips and tricks]. *IEEE Signal Processing Magazine*, 28(5):134–137, September 2011.

[32] SAOImage DS9 v7.2.1 software. Smithsonian Astrophysical Observatory, Center for Astrophysics, Harvard University.

[33] Glenn E. Healey. Radiometric CCD camera calibration and noise estimation. *IEEE Transactions on Pattern Analysis and Machine Intelligence*, 16(3):267–276, March 1994.

[34] Peter B. Stetson. A computer program for crowded-field stellar photometry. *Astronomical Society of the Pacific*, 99:191–222, March 1987.

[35] D. Freedman and P. Diaconis. *On the histogram as a density estimator: L2 theory*, volume 57, pages 453–476. 1981.

[36] Astropy Collaboration, T. P. Robitaille, E. J. Tollerud, P. Greenfield, M. Droettboom, E. Bray, T. Aldcroft, M. Davis, A. Ginsburg, A. M. Price-Whelan, W. E. Kerzendorf, A. Conley, N. Crighton, K. Barbary, D. Muna, H. Ferguson, F. Grollier, M. M. Parikh, P. H. Nair, H. M. Unther, C. Deil, J. Woillez, S. Conseil, R. Kramer, J. E. H. Turner, L. Singer, R. Fox, B. A. Weaver, V. Zabalza, Z. I. Edwards, K. Azalee Bostroem, D. J. Burke, A. R. Casey, S. M. Crawford, N. Dencheva, J. Ely, T. Jenness, K. Labrie, P. L. Lim, F. Pierfederici, A. Pontzen, A. Ptak, B. Refsdal, M. Servillat, and O. Streicher. Astropy: A community Python package for astronomy. *Astronomy & Astrophysics*, 558(A33), September 2013.

[37] E. Bertin. Source-Extractor: Program. Institut d Astrophysique & Observatoire de Paris.

[38] Steve B. Howell. Two-dimensional aperture photometry: Signal-to-noise ratio of point-source observations and optimal data-extraction techniques. *Astronomical Society of the Pacific*, 101:616–622, June 1989.

[39] S. M. Beard and H. T. MacGillivray. The COSMOS system for crowded-field analysis of digitized photographic plate scans. *Monthly Notices of the Royal Astronomical Society*, 247:311–321, 1990.

[40] Telescope data center, Smithsonian astrophysical observatory, Harvard university. http://tdc-www.harvard.edu/TDC.html.

[41] WCStools package, Smithsonian astrophysical observatory, Harvard university. http://tdc-www.harvard.edu/software/wcstools.html.

[42] Stephen E.; Canzian Blaise; Ables Harold D.; Bird Alan R.; Dahn Conard C.; Guetter Harry H.; Harris Hugh C.; Henden Arne A.; Leggett Sandy K.; Levison Harold F.; Luginbuhl Christian B.; Martini Joan; Monet Alice K. B.; Munn Jeffrey A.; Pier Jeffrey R.; Rhodes Albert R.; Riepe Betty; Sell Stephen; Stone Ronald C.; Vrba Frederick J.; Walker Richard L.; Westerhout Gart; Brucato Robert J.; Reid I. Neill; Schoening William; Hartley M.; Read M. A.; Tritton S. B. Monet, David G.; Levine. The USNO-B catalog. *The Astronomical Journal*, February 2003.

APPENDICES

A. Simulations Commands

A test file testx90m.fits is obtained from the on-line domain of Smithsonian Astrophysical Observatory [40] for the simulation. The WCSTools is used for fixing the WCS of the fits file and to obtain the catalog data of stars from the database. Along with the WCSTools, S-Extractor is also used for quickly locating certain number of bright stars. Following set of commands are executed (in the same order) in the UNIX environment.

At first, S-Extractor is used to locate sources in the image; their locations and the magnitudes. These locations and magnitudes of the sources are then listed in a file (for example star_ list.lst) and sorted in decreasing order of the magnitudes. In order to compare these informations with a catalog, a certain number of brightest stars are extracted and saved in another file (example, star_ list200.lst).

```
% Sorting and extracting 200 brightest stars
# sort -n -k 3 star_list.lst | head -200 > star_list200.lst
```

This list of 200 brightest stars is now used to match with data from one of the sky catalogs. The catalog used in this work is USNO-B1.0 (ub1) catalog. *ub1* has more than half a billion stars surveyed during last fifty years.
Finally, the corrected WCS is written into the same fits file after the match.

```
% Minimum number of matches set here is 50
# imwcs -vwd star_list200.lst -c ub1 -h 50 testx90m.fits
```

The following command retrieves x and y positions in the image along with other stellar informations (RA/Dec etc.) for 300 stars from the catalog.

```
# imcat -n 300 -w -c ub1 testx90m.fits
```

More details on using WCSTools could be found at [41].

B. Additional Plots

Effect of Iteration

For a synthetic image with $Z_o = 200$ ADU, $u_x = 6px, \sigma = 2px$, sky = 100 ADU and readout = 10 ADU, fig. B.1 shows the 2d plots of the estimated intensities after each iteration. Three iterations were enough for a fair estimate in this example.

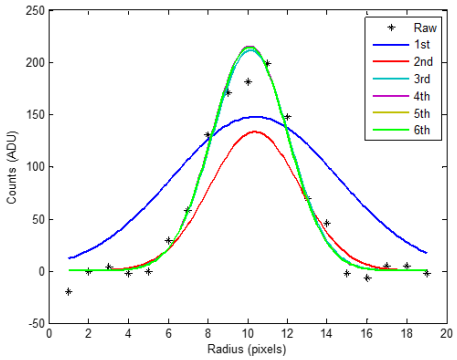

Figure B.1. Effect of iteration on the peak estimate. The bias present in the measurement model is minimized by iteration.

Log Plot

To illustrate how well the Gaussian approximation was, the following log-plot is generated. At first the measurement is normalized in 0-1 and then the estimate

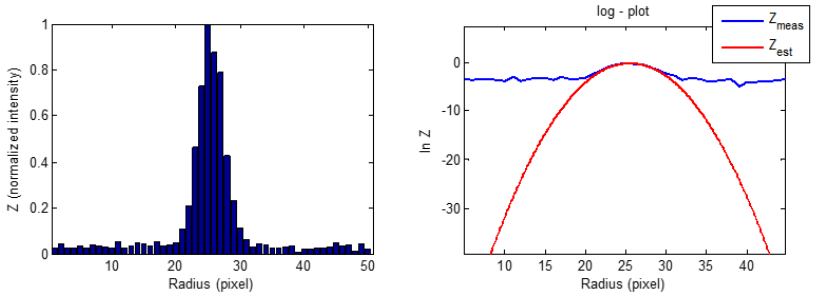

Figure B.2. Normalized intensity plot and the log-plot respectively

is made. As can be seen, the log-plot for the intensity estimate has the form of a parabola. Values which were significantly higher than 0 were approximated very well while those near 0 showed clear deviation.

Object's image was generated using the following data: $Z_o = 200$ ADU, $u_x = 6px, \sigma = 2px$, sky = 100 ADU and readout = 10 ADU.